Stony Brook University

Stony Brook University

Theory of ZnO and GaN: Nanostructures, Surfaces and Heterogeneous Photo-catalysis

A Dissertation Presented

by

Xiao Shen

to

The Graduate School

in Partial Fulfillment of the Requirements

for the Degree of

Doctor of Philosophy

in

Physics

Stony Brook University

August 2009

Stony Brook University

The Graduate School

Xiao Shen

We, the dissertation committee for the above candidate for the Doctor of Philosophy degree, hereby recommend acceptance of this dissertation.

Philip B. Allen – Dissertation Advisor
Professor, Department of Physics and Astronomy

Emilio E. Mendez – Chairperson of Defense
Professor, Department of Physics and Astronomy

Thomas T.S. Kuo
Professor, Department of Physics and Astronomy

Maria V. Fernandez-Serra
Assistant Professor, Department of Physics and Astronomy

James W. Davenport
Director, Computational Science Center, Brookhaven National Laboratory

James T. Muckerman
Senior Chemist
Brookhaven National Laboratory

This dissertation is accepted by the Graduate School.

Lawrence Martin
Dean of the Graduate School

Abstract of the Dissertation

Theory of ZnO and GaN: Nanostructures, Surfaces and Heterogeneous Photo-catalysis

by

Xiao Shen

Doctor of Philosophy

in

Physics

Stony Brook University

2009

A solid solution of wurtzite-structure GaN/ZnO absorbs light in the visible and can photo-split water. The photo-electrons reduce protons to H_2 when a co-catalyst is loaded. The photo-holes oxidize water into O_2 plus protons at the semiconductor-alloy/water interface. Microscopic details of the water oxidation process are unknown. This thesis focuses on water adsorption and oxidation on the surface of pure wurtzite GaN. A separate project on the relative stability of one-dimensional ZnO nanostructures is also included.

The first part of the thesis presents a study of water adsorption

on wurtzite GaN. The structures and energetics of a water monolayer adsorbed on the $(10\bar{1}0)$ nonpolar surface of GaN are studied computationally using density functional theory (DFT). Water is predicted to adsorb dissociatively, with protons attached to the surface N atoms and hydroxide ions attached to the surface Ga atoms. The calculated energy barrier for water dissociation is negligible.

The second part of this thesis presents a study of a possible reaction mechanism of water oxidation at the GaN-aqueous solution interface. A cluster model consisting of a fragment of the wet GaN surface is constructed. A few explicit water molecules and a polarizable continuum model are used to simulate the aqueous environment. Based on calculations on the cluster model using hybrid DFT-Hartree Fock theory, we propose a four-step mechanism for water oxidation. It starts at the hydroxide ion attached to a surface Ga atom, and consists of four proton-coupled electron transfer reactions. Key intermediates and the rate-limiting step are identified.

The last part of this thesis is dedicated to a separate project on the relative stability of ultrasmall ZnO one-dimensional nanostructures. The energies of ZnO nanowires and single-walled nanotubes with n atoms per periodic unit are calculated at the DFT-LDA (local density approximation) and GGA (generalized gradient approximation) level of theory. The nanotubes are found to be lower in energy when n is small.

This thesis is dedicated to my parents and grandparents.

Contents

List of Figures

List of Tables

Preface

This thesis is organized as following: Chapter 1 gives the background information and an overview of the presented research. Chaptor 2 gives a brief introduction to the methods, including density functional theory and hybrid density functional theory, Gaussian basis set, polarizable continuum model, and a short review of electrochemistry. Chapter 3 studies the water adsorption on the GaN $(10\bar{1}0)$ surface. It is a reproduction of the paper published in the Journal of Physical Chemistry C. My coauthors are Philip B. Allen, Mark S. Hybertsen and James T. Muckerman. All the computation and the major part of the writing were done by me. Chapter 4 presents a study of water oxidation pathway on GaN $(10\bar{1}0)$ surface, which hasn't been published at the moment, but has been edited by Philip B. Allen and James T. Muckerman. Chapter 5 contains a study of the relative stability of 1D ZnO nanostructures. It is a reproduction of the paper published in Nano Letters. My coauthors are Philip B. Allen, James T. Muckerman, James W. Davenport and Jin-Cheng Zheng. All the computation and the major part of the writing were done by me. I thank my coauthors for helping edit the papers and for permission to include them in the thesis.

Acknowledgements

I thank my advisor Prof. Philip Allen for his encouragements and tireless mentoring. I thank Prof. Marivi Fernandez-Serra, Dr. Mark Hybertsen and Dr. James Muckerman for invaluable advice and inspiring discussions. I thank Prof. Jin-Cheng Zheng for introducing me to the practice of density functional theory calculations. I thank Dr. James Davenport for hosting me at Brookhaven National Lab and helping me on computations. I thank Dr. Marshall Newton, Dr. Mark Pederson and Dr. Qin Wu for helpful discussions. I thank my fellow graduate students and postdocs: Dr. Linlin Jensen, Dr. Wei Kang, Li Li, Dr. Yolanda Small, Dr. Tao Sun, Meagan Thompson and Jue Wang, for their help and support. I thank Leonard Slatest and Stratos Efstathiadis for their assistance on the New York Blue supercomputer. The works are supported by Stony Brook/BNL seed grant, Brookhaven Science Associates LLC 1D#129988 (via CFN), and DOE grant #DEFG0208ER46550.

The text of this thesis contains materials which have been previously published in the following articles.

X. Shen, P. B. Allen, J. T. Muckerman, J. W. Davenport, and J.-C. Zheng,

Wire versus Tube: Stability of Small One-Dimensional ZnO Nanostructures

Nano Letters **7**, 2267 (2007),

X. Shen, P. B. Allen, M. S. Hybertsen, and J. T. Muckerman, *Water Adsorption on the GaN* $(10\bar{1}0)$ *Nonpolar Surface*

Journal of Physical Chemistry C **113**, 3365 (2009),

electron-hole pairs:

$$4h\nu \rightarrow 4e^- + 4h^+$$

Then, two half-reactions happen:

$$4H^+ + 4e^- \rightarrow 2H_2$$

$$2H_2O + 4h^+ \rightarrow O_2 + 4H^+$$

One half-reaction is the proton reduction, where photo-electrons reduce the protons in the aqueous solution into H_2 molecules; the other half-reaction is the water oxidation, where photo-holes oxidize water molecules and produce O_2 molecules and protons.

For a semiconductor to be a photocatalyst for overall water splitting, it must satisfy the following requirements:

1. It must be stable during the reaction.

2. Its conduction-band-edge must lie lower than the standard reduction potential of the proton reduction reaction, so the photo-electrons have enough energy to reduce the protons;

3. Its valence-band-edge must lie higher than the standard reduction potential of the water oxidation reaction, so the photo-holes have enough energy to oxidize water molecules;

4. To effectively use the solar energy, the semiconductor should have a suitable band gap to capture the visible part of the solar spectrum, which contains more energy than the UV part of the solar spectrum.

So far, not many materials satisfy all these requirements. One of them is

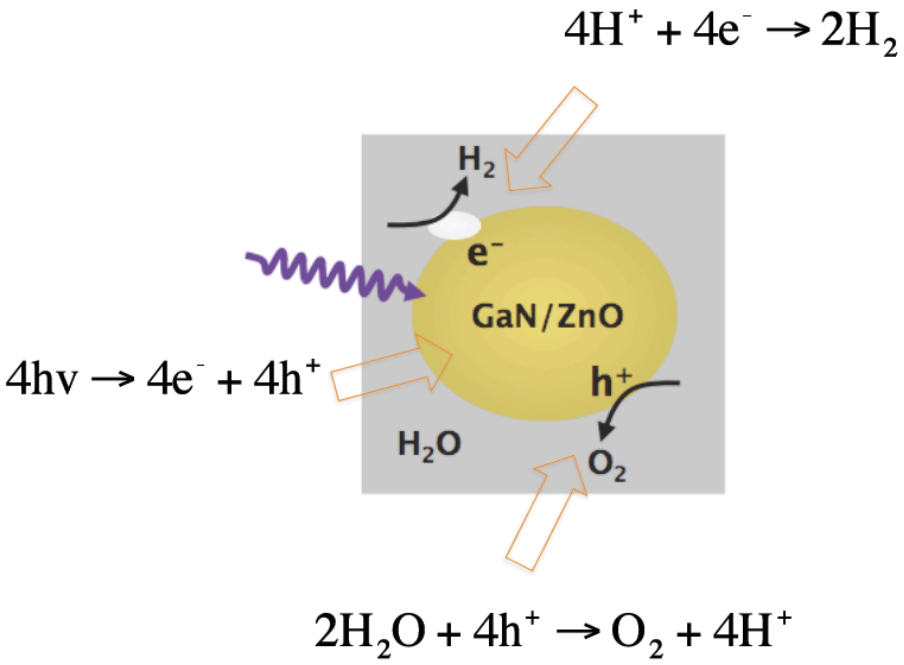

Figure 1.1: Schematic view of Domen's photocatalyst at work. Light (purple wavy line) comes in and generates electrons and holes. The electrons come to the co-catalyst site(white particle) and reduce protons into H_2. The holes come to the surface of the GaN/ZnO solid solution, oxidizing water into O_2. (Figure made by Mark S. Hybertsen. Used with permission.)

the solid solution of GaN and ZnO, which is the material we are studying. More details about this solid solution will be given in the next section.

1.2 GaN/ZnO Solid Solution Photocatalyst

In 2005, Domen's group synthesized a solid solution of GaN and ZnO[1]. This GaN/ZnO solid solution plays two roles in the photo-splitting of water. First, it absorbs light and provides photo-electrons and photo-holes. Second, its surface also acts as a good catalyst for water oxidation. This solid solution

$Ga_{1-x}Zn_xN_{1-x}O_x$ is made by nitriding a mixture of Ga_2O_3 and ZnO under NH_3 flow. The value of x is between 0.05 and 0.42[2, 3]. The synthesized solid solution is a yellow powder whose band gap is estimated to be between 2.43 and 2.8 eV,[2, 3] which is smaller than both GaN (3.4 eV) and ZnO (3.2 eV). A first-principles study has predicted the minimum band gap to be 2.29 eV at $x = 0.525$[4]. The narrowing of the band gap is believed to be due to the rise of the valence band maximum (mainly N 2p states), which is caused by their repulsion from the lower lying Zn 3d electrons[1, 5]. Because of the lowered band-gap, this solid solution is able to absorb visible light.

When a co-catalyst for proton reduction (the best one so far is nanoparticles of $Rh_{2-x}Cr_xO_3$ mixed oxide) is loaded onto the surface of the GaN/ZnO solid solution, this solid solution works as an over-all water-splitting photocatalyst. The process of water-splitting is shown in Fig 1.1. The highest achieved quantum efficiency (defined as the ratio of photo-excitations used in the reaction to the photons absorbed by the photocatalyst) for overall water splitting is 5.9%[6].

Of the two half reactions, proton reduction can be done efficiently with known catalysts such as Pt metal, but efficient water oxidation catalysts are not readily available. Therefore, it is exciting that Domen finds that the water oxidation reaction on the surface of GaN/ZnO solid solution is very efficient. When the proton reduction reaction is short-circuited by using Ag^+ as sacrificial reagent, high quantum efficiency (51%) is achieved for water oxidation[3].The 51% quantum efficiency means that, for every two photoholes generated in the solid solution, one is used to oxidize water. Before our work, there was no knowledge about the atomic details of this water oxidation

reaction. Water oxidation is not the bottleneck for the efficiency of overall water-splitting in the Domen cell, but it has been the bottleneck in previous schemes. Therefore, it is interesting to know how water oxidation happens on the surface at the atomic level of detail, and understand why the efficiency is so high. This knowledge will have both practical value for searching and designing new materials as photo-catalysts or photo-anodes[7] for solar water-splitting, and also will have fundamental importance for our understanding of heterogenous catalysis in its own right.

1.3 Project Overview

As stated above, our goal is to understand the water oxidation mechanism on the surface of GaN/ZnO solid solution in atomistic detail. We attack this problem by computational modeling. A full understanding of this heterogeneous photo-catalytic process should include (but is not limited to) the answers to the following four questions:

(1) Which surface or surface site is relevant to water oxidation?

(2) What is the structure of the semiconductor/aqueous solution interface?

(3) What is the reaction pathway and what are the key intermediates?

(4) How do photo-holes tranfer from the solid solution to the water moieties?

The first question is one of the most important ones in heterogeneous catalysis, and is also the first question we have to face in our theoretical modeling. However, current experiments provide no answer. Domen's solid solution photocatalyst samples consist of large nanoparticles of irregular shapes, with all

kinds of surfaces, steps, edges, and very likely, surface defects. His experiments didn't tell us where the water oxidation happens. This question can only be answered either by future experiments, or by the accumulation of knowledge from theoretical studies on a few specific cases, or by a combination of these two. Our strategy is to choose one well-defined surface and start our investigations. In this way, we will not only learn about the physics and chemistry in this system, but also test our theoretical approaches and computational tools.

We have chosen the non-polar $(10\bar{1}0)$ surface of pure wurtzite GaN to be our model system. This choice is based on the following facts: (1) Pure wurtzite GaN is also an overall water-splitting photocatalyst which works in UV, and also shows high quantum efficiency for water oxidation when the proton reduction half-reaction is short-circuited[8]. (2) The $(10\bar{1}0)$ surface is one of the most stable surfaces of GaN, as it often appears as the inside wall of nanopipe defects[9–13]. (3) The structure of a monolayer of water on the same $(10\bar{1}0)$ surface of pure ZnO has been studied by both experiment and theory[14], and an interesting half-dissociation structure is discovered. It will be interesting to compare the structures of water on the same $(10\bar{1}0)$ surface of GaN and ZnO. We also have some experience on this ZnO $(10\bar{1}0)$ surface from our previous work on ZnO nanowires.

The second question is about the starting point of the reaction. It can be asked at two levels. At the first level, the question is, what is the ground-state structure of a monolayer of water at the surface? Density functional theory (DFT) is usually the method of choice for this kind of problem. For the GaN $(10\bar{1}0)$ surface, this question is answered by us[15], and the work will be presented in Chapter 3 of this thesis. The second level is closer to

reality: what is the structure of the semiconductor/aqueous solution interface at finite temperature? First-principles molecular dynamics, where the forces are generated by using density functional theory, is the method of choice for this kind of problem. Answering the second level of question is the research project of one of my colleagues (Jue Wang), and it will not be presented in detail in this thesis.

The third question is about finding possible stable intermediates and the reaction steps connecting them. It also implies that the energetics should be examined to make sure that the proposed reaction pathway makes sense in reality. Finding the intermediates and pathway is a process relying on both computer experiments and chemical knowledge and intuition. After those intermediates are found and a pathway connecting them is constructed, the Gibbs free energies of these intermediates are calculated. Our approach uses the "hybrid density functional theory" to obtain more accurate electronic structures and energetics, and uses a combination of explicit water molecules and a polarizable continuum model to properly describe the aqueous environment. (The details of hybrid density functional theory and polarizable continuum model will be explained in Chapter 2.) This approach has been used for homogeneous catalysis. This thesis is the first use of the polarizable continuum model for a heterogeneous catalysis problem. For the GaN $(10\bar{1}0)$ surface, we now have a fairly complete and consistent hypothesis about the intermediates, reaction pathways, and the energetics. This work will be presented in Chapter 4.

The fourth question is about further details along the reaction pathway. In a sense, question (3) only asks for the starting and end points for each step, while question (4) asks about how and how fast to go from one point

to another. The high efficiency of water oxidation on the surfaces of the GaN/ZnO solid solution and pure GaN might only be explained when our understanding reaches this level. However, this is beyond the scope of this thesis.

In summary, our goal is to understand the mechanism of water oxidation on the surface of the GaN/ZnO solid solution photocatalyst with atomistic detail. Initial steps to pursue this goal are presented in this thesis. For the four important questions in understanding this heterogeneous photo-catalytic process, the work presented in this thesis bypasses the first one by choosing a specific surface (the $(10\bar{1}0)$ surface of pure wurtzite GaN) to model, provides answers to the second and third questions for that model system, and makes no attempt to answer the fourth question. The knowledge learned from this specific model surface, and the methods employed here, should be valuable for the studies of other surfaces, and for investigations in greater detail.

Chapter 2

Methods

2.1 Density Functional Theory

Realistic modeling of solids and molecular systems often requires solving the many-body Schrödinger equation of n interacting electrons in an external field. In this thesis, we use the density functional theory (DFT). Its basics are described below.

2.1.1 Foundations

Density functional theory is based on the Hohenberg-Kohn theorems[16] and the Kohn-Sham ansatz[17]. The Hohenberg-Kohn theorems state that for a many-body system, there exists a one-to-one correspondence between the external field $V_{\text{ext}}(r)$ and the ground state electron density $\rho(r)$. Furthermore, a functional for the energy $E[\rho]$ can be defined in terms of ρ. For a given $V_{\text{ext}}(r)$, the ground state energy of the many-body system corresponds to the global minimum of $E[\rho]$, and the corresponding ρ is the ground state density. $V_{\text{ext}}(r)$

contains all one-electron potentials (like $-Ze^2/|r-R|$) in the Schrödinger equation. The interaction $e^2/|r-r'|$ is the hard part which DFT is avoiding solving directly. The Kohn-Sham ansatz says that the interacting many-body system can be replaced by a fictitious auxiliary non-interacting system with single electron eigenstates $\psi_i(r)$ and with the same density, $\rho = \sum_{\epsilon_i \leqslant \epsilon_F} |\psi_i(r)|^2$. The ground state energy of the interacting system $E[\rho]$ is then the same as the ground state energy of the non-interacting system $E_{\mathrm{KS}}[\rho]$, which can be expressed as:

$$E_{\mathrm{KS}}[\rho] = T[\rho] + \int d^3r [V_{\mathrm{ext}}(r)\rho(r) + E_{\mathrm{Hartree}}[\rho] + E_{xc}[\rho]] \ .$$

Here $T[\rho]$ is the kinetic energy of the fictitious non-interacting electrons. The second term is the potential energy of electrons due to the external field. $E_{\mathrm{Hartree}}[\rho]$ is the direct Coulomb interaction energy between the electrons. The last term $E_{xc}[\rho]$ is the exchange-correlation energy which contains all the many-body effects of exchange and correlation, and is a functional of the electron density ρ . The exact form of $E_{xc}[\rho]$ is unknown.

2.1.2 LDA and GGA

There are various ways to approximate the $E_{xc}[\rho]$. One of them is the local density approximation (LDA). This approximation says that for a slowly varying density $\rho(r)$, the total exchange-correlation energy can be written as:

$$E_{xc}^{\mathrm{LDA}} = \int d^3r \rho(r) \epsilon_{xc}^{\mathrm{LDA}}(\rho(r)) \ .$$

Here the exchange-correlation energy density $\epsilon_{xc}^{\mathrm{LDA}}(\rho(r))$ is equal to the ϵ_{xc} of a homogeneous electron gas with the same electron density. The exchange-correlation energy density $\epsilon_{xc}^{\mathrm{LDA}}$ is usually divided into the exchange energy density $\epsilon_x^{\mathrm{LDA}}$ and the correlation energy density $\epsilon_c^{\mathrm{LDA}}$. The $\epsilon_x^{\mathrm{LDA}}$ term takes the analytic form of the exchange energy of the homogeneous electron gas, $\epsilon_x = -\frac{3e^2}{4}(\frac{3}{\pi})^{1/3}\rho^{1/3}$ (assuming the electron gas is not spin-polarized)[18]. For $\epsilon_c^{\mathrm{LDA}}$, since the correlation energy density has an unknown algebraic form in the case of the homogeneous electron gas, the formulas for $\epsilon_c^{\mathrm{LDA}}$ are often obtained by parameterizing the numerical results, for example, the quantum Monte Carlo results obtained by Ceperley and Alder[19]. Two examples of the parameterized expression of $\epsilon_c^{\mathrm{LDA}}$ are the Perdew-Zunger (PZ) form[20] (used in Chapter 5) and the Vosko-Wilk-Nusiar (VWN) form[21].

An improvement over the LDA is the generalized gradient approximation (GGA), in which the exchange-correlation energy density depends not only on the density of the electrons, but also the gradient of the density. Two of the most popular forms of GGA are the Perdew-Burke-Ernzerhof (PBE) form (used in Chapter 3 and 5)[22] and the Becke-Lee-Yang-Parr (BLYP) form[23–25].

2.1.3 Hybrid Density Functional Theory

Comparison with data, especially in molecules, reveals deficiencies in all known attempted forms of $E_{xc}[\rho]$. It is believed that the exchange energy (which in Hartree-Fock theory is NOT a functional of ρ) may be the worst problem. Therefore, an improvement of the density functional is attempted (which

abandons strict Hohenberg-Kohn theorems) by mixing the LDA and GGA exchange-correlation functionals with the orbital-dependent Hartree-Fock exact exchange functional[26]. One example is the popular B3LYP hybrid functional[23, 24, 27] (used in Chaper 4), which can be written as:

$$E_{xc} = E_x^{\mathrm{LDA}} + a_0(E_x^{\mathrm{HF}} - E_x^{\mathrm{LDA}}) + a_x(E_x^{\mathrm{Becke}} - E_x^{\mathrm{LDA}}) + a_c(E_c^{\mathrm{LYP}} - E_c^{\mathrm{LDA}}) \ .$$

Here the E_x^{Becke} is the Becke exchange functional[23], E_c^{LYP} is the Lee-Yang-Parr correlation functional[24], and E_c^{LDA} takes the VWN form[21]. The three parameters $a_0 = 0.20$, $a_x = 0.72$, and $a_c = 0.81$ were originally obtained by empirically fitting to the atomic and molecular data using the PW91 correlation functional[28].

The hybrid density functionals often not only yield better energetics, but also lead to other improvements, such as better band gaps in solids and better descriptions of localized states.

2.2 Gaussian Basis Set

2.2.1 Slater-type and Gaussian-type functions

The single-electron eigenstates in Kohn-Sham ansatz are usually expanded in a set of basis functions such as plane-waves or a localized basis set. Among localized basis sets, the Gaussian-type functions and Slater-type functions are popular. A Slater-type function decays as $e^{-\zeta r}$, and a Gaussian-type function decays as $e^{-\alpha r^2}$. The advantage of Slater-type functions is that they represents the atomic orbitals better than Gaussian type functions, so high quality basis

can be constructed by using a small number of functions. The disadvantage of Slater-type function is that the multi-center integrals (such as the Coulomb and exchange matrix elements in Hartree-Fock equations) have to be calculated numerically, which can limit their utility. Gaussian functions have the advantage that the product of two Gaussians is also a Gaussian, so that all the multi-center integrals can be evaluated analytically. The disadvantage of Gaussians is that they poorly represent the atomic orbitals. To construct an atomic orbital, a number of Gaussian functions are required.

2.2.2 Contracted Gaussian

To overcome the problem of Gaussian functions while maintaining their advantage, practical calculations usually use contracted Gaussian-type orbitals (CGTOs). CGTOs are fixed linear combinations of Gaussian functions (also called primitive Gaussians) and can be made to simulate Slater-type orbitals (STO) or other types of functions. For every CGTO, the exponent and coefficients of the primitive Gaussians are fixed during the calculation. The scheme of contraction is often written as (# of primitive Gaussians)/[# of CGTOs]. For example, the (4s)/[2s] notation means that two s-type CGTOs are obtained by contracting 4 s-type primitive Gaussians.

2.2.3 Double Zeta Basis Set

One can use one CGTO for each orbital (also called single zeta). However, this basis lacks of flexibility. The first step of improvement is done by using a linear combination of two basis functions (CGTOs) for one orbital. This is called

double zeta (double-ζ) basis. The orbital exponents of these two CGTOs are slightly above and below the optimal value in the single-zeta basis, and the linear combination coefficient of the two CGTO are allowed to vary depending on the chemical environment. The double zeta basis sets can be further divided into two kinds: full double zeta basis sets and valence double zeta basis sets. In a full double zeta basis set, the wave function of each orbital is expanded into two CGTOs. In a valence double zeta basis set, the atomic orbitals are divided into an inner shell and a valence shell. Only one CGTO is used for an inner-shell orbital, and two CGTOs are used for a valence-shell orbital. The D95 basis set used in Chapter 4 is a full double zeta basis set. For first-row atoms like oxygen, its contraction scheme can be expressed as (9s5p)/[4s2p], where 4 s-type CGTOs (2 for the 1s orbital, and 2 for the 2s orbital) are made by combining 9 s-type primitive Gaussians; and 2 p-type CGTOs (for 2p orbital) are made by combining 5 p-type primitive Gaussians[29]. The D95V basis set (used in Chapter 4 together with the LANL2 effective core potential) is a valence double zeta basis set. For first row atoms, it uses 1 CGTO for the 1s (inner shell) orbital, and uses 2 CGTOS for the 2s and 2p orbitals (valence shell). Its contraction scheme can be expressed as (9s5p)/[3s2p][30].

2.3 Polarizable Continuum Model

2.3.1 PCM and C-PCM/COSMO

Polarizable continuum models[31] are useful ways to describe solute-solvent interactions. In a polarizable continuum model, a dielectric continuum is used

to simulate the solvent. The molecule (solute) is placed into a void cavity in the continuum. The interaction of the solvent to the solute is expressed as a polarization charge density on the cavity surface.

There are various versions of polarizable continuum models. In this thesis, the conductor-like solvation model (COSMO or C-PCM)[32] is used. In this model, the solvent is treated like a conductor, and the potentials due to the polarization charge and the solute molecule cancel out at the surface. Using this boundary condition, the ideal unscreened surface charge density is calculated. This ideal unscreened surface charge density is then scaled to recover the effect of the finite dielectric constant of the solvent. The total energy of the solute molecule, including the electrostatic interaction between the solute and solvent, can be minimized in a self-consistent manner, and yields the electrostatic energy G_{es}. (See below).

2.3.2 Solvation Energy

The total free energy of a molecule in solvent can be written as

$$G = G_{\text{es}} + G_{\text{cav}} + G_{\text{dis-rep}} \ .$$

The first term G_{es} in the electrostatic energy, which includes the electrostatic interaction between the solute and solvent. The second term G_{cav} is the cavity formation energy. It can be calculated in a number of ways. One example is to express it as $G_{\text{cav}} = \sum_i \frac{A_i}{4\pi R_i^2} G_i^{\text{HS}}$, where A_i is the area of the ith sphere exposed to the solvent, R_i is the radius of the ith sphere, and G_i^{HS} is the cavity formation energy for of a sphere with radius R_i in a fluid of hard spheres[33].

The third term $G_{\mathrm{dis-rep}}$ is the dispersion-repulsion energy. There are various ways to evaluate this term. One example is the procedure described in Refs. [34, 35], where atom-atom potential parameters[36] are used.

2.3.3 The Cavity Surface

There are three definitions of cavity surfaces, as shown in Fig. 2.1:

(1) The van der Waals surface (VWS) is the surface obtained by the combination of spheres centered on atoms or atomic groups of the solute with the radii equal to the van der Waals radii. This surface is used in calculating G_{cav}.

(2) The solvent accessible surface (SAS) is defined as the set of points which correspond to the center of a spherical solvent molecule as it rolls on the VWS. This surface is used to calculate $G_{\mathrm{dis-rep}}$.

(3) The solvent excluded surface (SES) is defined as the surface of the tangent points as a spherical solvent rolls on the VWS. This surface is used to calculate G_{es}. In practice, this surface is usually approximated by adding spheres to the VWS surface[38–40]. (In this case, the vdW radii are usually scaled by a factor $f > 1$.)

2.3.4 Determination of the Radii

To obtain more accurate solvation energies, optimized van der Waals radii are often used. These optimized radii are determined as follows.

Each non-hydrogen atom has a basic radius, (the hydrogens have no individual spheres, and are included in the spheres of the attached atoms), and corrections to the basic radius are determined by the number of hydrogens it

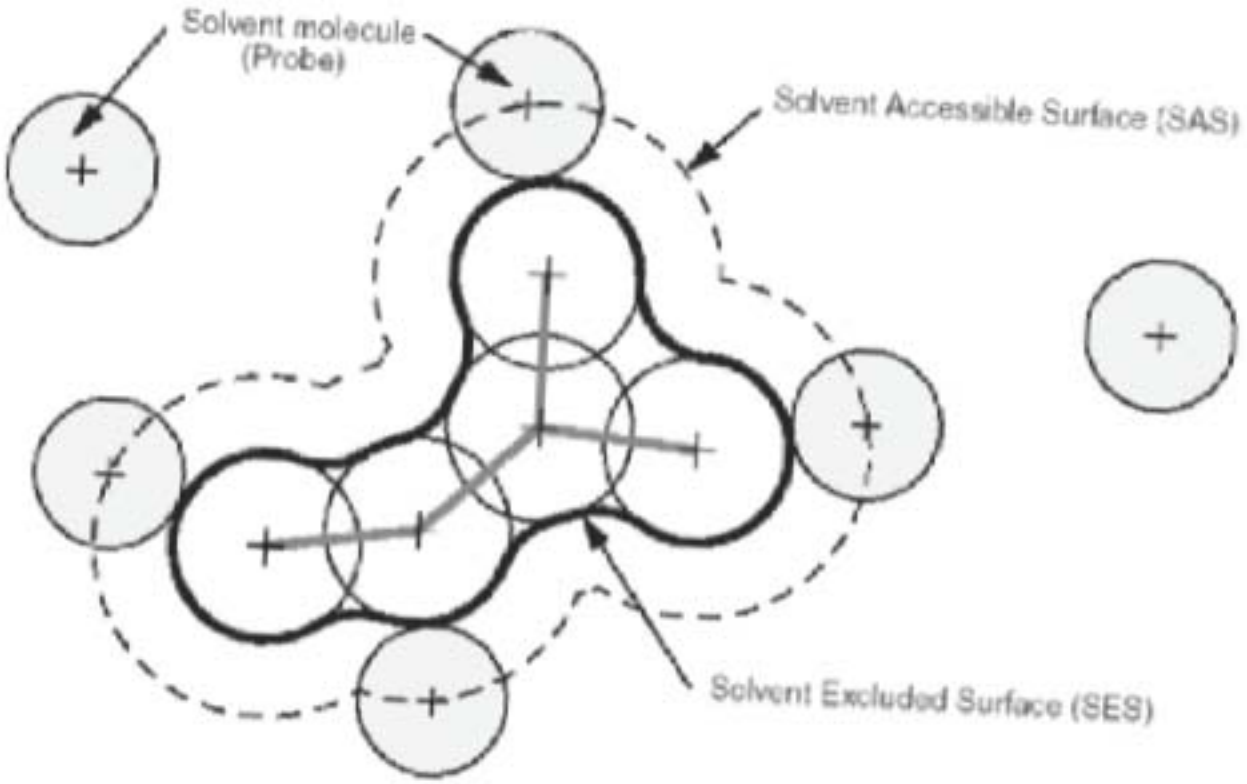

Figure 2.1: Illustration of cavity surfaces. The van der Waals surface (VWS) is made of the spheres centered at the nuclei (shown as +). The solvent accessible surface (SAS) is shown as the dashed line. The solvent excluded surface (SES) is shown as thick black line. (Figure taken from Ref. [37]. Used with permission.)

bonds to, the hybridization, charge, and the nature of its nearest neighbors. When the parameters in the corrections are optimized for Hartree-Fock theory, the corresponding radii are called united-atom Hartree-Fock (UAHF) radii[41]. When the parameters in the corrections are optimized for hybrid DFT theory (using the PBE0 functional), the corresponding radii are called united-atom Kohn-Sham (UAKS) radii[42].

2.4 Review of Electrochemistry

2.4.1 Cell Potential and Free Energy

Let us recall that there are two kinds of electrochemical cells. One is the Galvanic cell, the other is the electrolytic cell. Examples are shown in Fig. 2.2. Each cell contains two electrodes. One is the cathode, at which the reduction reaction takes place. The other is the anode, at which the oxidation reaction takes place. The difference between these two kinds of cells is that, for a Galvanic cell, the cell reaction will happen spontaneously when the two electrodes are connected by a conductor; while for a electrolytic cell, an external power supplied is required to drive the cell reaction; otherwise the reaction will not happen.

For each cell, we can define the cell potential. Let us take the Galvanic cell in Fig. 2.2a as an example. We can write the cell reaction in its compact form: $Zn|Zn^{2+}||Cu^{2+}|Cu$. The reduction reaction (at the cathode) is written on the right by convention. The cell potential E is defined as the potential of the right electrode relative to the left electrode.

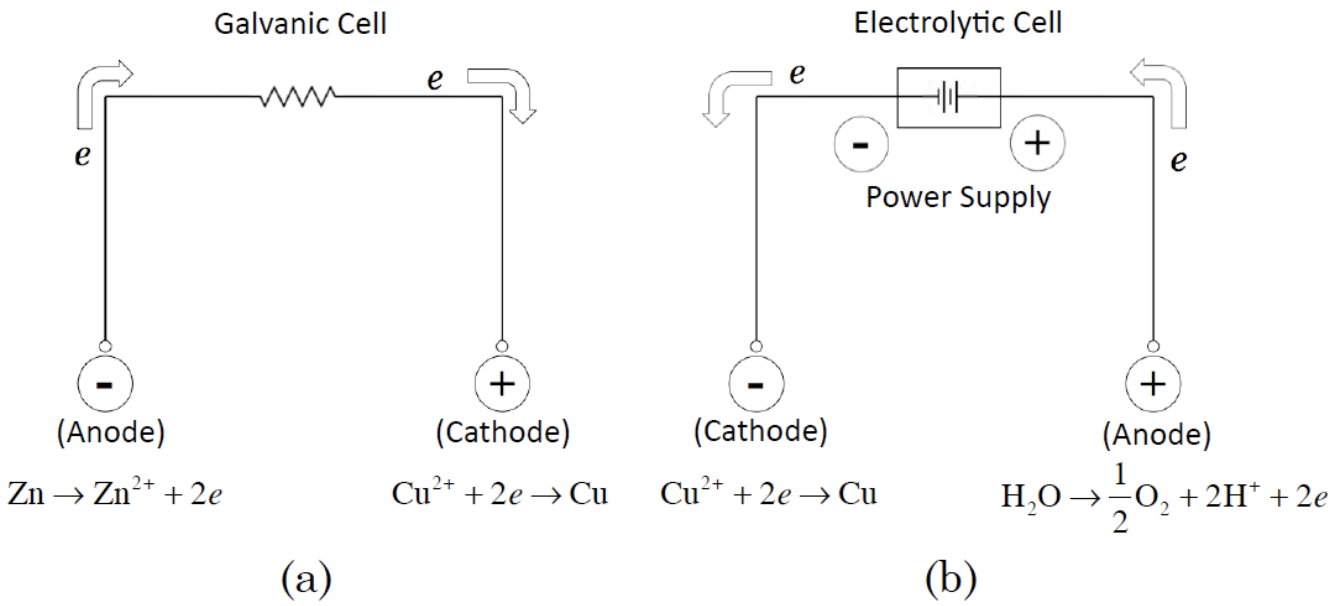

Figure 2.2: Examples of electrochemical cells. (a): a Galvanic cell, (b): an electrolytic cell

The absolute value of the free energy change in the cell ΔG is also the maximum amount of work it can do to the external circuit. It can be related to the maximum cell potential E by the relation $\Delta G = -nFE$, where n is the amount of charge transfered in the circuit and F is the Faraday constant. The negative sign in the above formula comes from the convention that for a spontaneous cell reaction, $\Delta G < 0$ and $E > 0$

2.4.2 Electrode Potential and Reduction Potential

Oftentimes we are only interested in the property of one electrode. This electrode is often called "working" electrode. Its potential can be measured against a reference electrode. Historically, the normal hydrogen electrode (NHE), also called standard hydrogen electrode (SHE) is chosen to be the reference and its potential is chosen to be zero. At the NHE, gas phase H_2 at 1 atm partial pressure (at 298.15K) is in equilibrium with protons in aqueous solution with unit activity. (Activity a of a chemical species is defined as $a = \exp(\frac{\mu-\mu^o}{RT})$, where μ is the chemical potential of the species, and μ^o is the standard state chemical potential, R is the ideal gas constant, T is the temperature. Unit activity means $\mu = \mu^o$.) Since NHE is hard to realize experimentally, in practice the potentials of working electrodes are often measured using other reference electrodes, such as reversible hydrogen electrode (RHE), saturated calomel electrode (SCE) and silver/silver chloride electrode.

The electrostatic potential of an electrode (relative to NHE), where the oxidized species Ox and the reduced species Red are in equilibrium, is always equal to the cell potential of a cell where the reduction reaction $\text{Ox}+ne \rightarrow \text{Red}$

happens at the cathode and the oxidation reaction $H_2 \rightarrow 2H^+ + 2e$ happens at the NHE anode. So the electrode potential is also the potential for the reduction half-reaction, and it is also called the "reduction potential". When all species are at their standard state, the potential E becomes "standard electrode potential" or "standard reduction potential" E°.

The standard reduction potential shows how easy (or how hard) a reduction or oxidation reaction is. The more positive the standard reduction potential, the harder the oxidation reaction is, and generally speaking, the reduced form of the species is more stable. An example is $E^{\circ}_{Au^+/Au} = 1.83$ V , which is very positive. This means that to oxidize Au to Au^+ is difficult and the reduced form Au is more stable. The more negative the standard reduction potential, the harder the reduction reaction is, which means that the oxidized form of the species is more stable. An example is $E^{\circ}_{Li^+/Li} = -3.045$ V , which is very negative. This means that reducing Li^+ to Li is difficult, and the oxidized form Li^+ is more stable.

For photo-splitting of water, the standard reduction potential for proton reduction $E^{\circ}_{H^+/H}$ is equal to 0 by definition, while standard reduction potential for O_2 reduction (reverse reaction of water oxidation) $E^{\circ}_{O_2/H_2O}$ is equal to 1.23 V (experimental value). For a water-splitting semiconductor photocatalyst, in the proton-reduction half-reaction, the electrons comes from the conduction band, so the conduction-band-edge potential of the semiconductor must be more negative than the proton reduction potential. In the water-oxidation half reaction, the holes comes from the valence band, so the valence-band-edge potential of the semiconductor must be more positive than the O_2 reduction potential.

2.4.3 Calculating the Standard Reduction Potential

To calculate the standard reduction potential of the reaction

$$\mathrm{Ox} + e \rightarrow \mathrm{Red}$$

we can add an NHE anode (where the reaction $\frac{1}{2}\mathrm{H_2} \rightarrow \mathrm{H^+} + e$ happens) to it and make an hypothetical electrochemical cell. The total reaction of the cell is

$$\mathrm{Ox} + \frac{1}{2}\mathrm{H_2} \rightarrow \mathrm{Red} + \mathrm{H^+}$$

Once the change of the standard state free energy of the whole cell ΔG^{o} is known, the standard reduction potential E^{o} can be calculated by the relation

$$\Delta G^{\mathrm{o}} = -nFE^{\mathrm{o}}$$

ΔG^{o} can be calculated as

$$\Delta G^{\mathrm{o}} = \Delta G^{\mathrm{o}}_{\mathrm{O/R}} + \Delta G^{\mathrm{o}}_{\mathrm{NHE}}$$

$$\Delta G^{\mathrm{o}}_{\mathrm{O/R}} = G^{\mathrm{o}}_{\mathrm{s}}(\mathrm{R}) - G^{\mathrm{o}}_{\mathrm{s}}(\mathrm{O})$$

$$\Delta G^{\mathrm{o}}_{\mathrm{NHE}} = G^{\mathrm{o}}_{\mathrm{s}}(\mathrm{H^+}) - \frac{1}{2}G^{\mathrm{o}}_{\mathrm{g}}(\mathrm{H_2})$$

where $G^{\mathrm{o}}_{\mathrm{s}}(\mathrm{O})$, $G^{\mathrm{o}}_{\mathrm{s}}(\mathrm{R})$, and $G^{\mathrm{o}}_{\mathrm{g}}(\mathrm{H_2})$ are standard state Gibbs free energies of the species Ox, Red, and $\mathrm{H_2}$, which can be obtained from first-principles calculations. $G^{\mathrm{o}}_{\mathrm{s}}(\mathrm{H^+})$ is the standard state free energy of a proton, which is obtained using the experimental data, since no reliable theoretical value is

available. (Here the superscript "o" denotes a standard state, the subscripts "g" and "s" denote the gas phase and the aqueous phase, respectively. A more detailed notation will be used in Chapter 4.)

The Gibbs free energy G is calculated as:

$$G = U + PV - TS$$

where U is the internal energy, which can be written as

$$U = E_{\mathrm{SCF}} + E_{\mathrm{thermal}} = E_{\mathrm{SCF}} + E_{\mathrm{el}} + E_{\mathrm{tran}} + E_{\mathrm{rot}} + E_{\mathrm{vib}}$$

and the entropy term S can be written as

$$S = S_{\mathrm{el}} + S_{\mathrm{tran}} + S_{\mathrm{rot}} + S_{\mathrm{vib}}$$

here E_{SCF} is the electronic ground state energy of the species. E_{el}, E_{tran}, E_{rot}, and E_{vib} are the thermal corrections to energy due to electronic excitations (neglected because the electronic excitation energy is assumed to be much larger than $k_B T$), translations, rotations, and vibrations (including the zero-point energy). Similarly, S_{el}, S_{tran}, S_{rot}, and S_{vib} are the electronic (neglected), translational, rotational, and vibrational entropies. E_{tran}, E_{rot}, S_{tran}, and S_{rot} can be easily calculated given the mass and moments of inertia of the species[43]. E_{vib} and E_{vib} can be calculated once we have obtained the vibrational frequencies of the normal modes from first-principle calculations.

Chapter 3

Water Adsorption on GaN $(10\bar{1}0)$ surface

3.1 Introduction

GaN is a technologically important material that appears in the wurtzite phase in bulk, films, and nanostructures. Domens group discovered that particles of a solid solution of wurtzite GaN and ZnO, when loaded with a cocatalyst for proton reduction, can absorb light in the visible range and can photosplit water into H_2 and O_2[3]. First-principles calculations help explain the enhanced visible-light absorption of the $(Ga_{1-x}Zn_x)(N_{1-x}O_x)$ solid solution[4]. It is believed that H_2O is oxidized by photoholes at the GaN/ZnO surface. However, the microscopic details are unclear. Little is known about either the geometries or the compositions of the alloy surfaces, and it is hard to tell from the experimental data where and how the reaction occurs. First principles calculations have also provided valuable information about water adsorption on the

ZnO $(10\bar{1}0)$ surface[14, 44–46]. Inspired by these previous studies, this paper begins to address the complicated water oxidization problem by answering a narrower question: How does a monolayer of water adsorb on the surface of pure GaN?

Domen's experiments do not identify which surface accounts for the O_2 generation. Experiments on water adsorption have been carried out on the polar (0001) surface of GaN on which ca. 60% of the water molecules are found to adsorb dissociatively[47]. We focus on the nonpolar $(10\bar{1}0)$ GaN surface in this study. The $(10\bar{1}0)$ surface is the most stable surface of ZnO[48]. The GaN $(10\bar{1}0)$ surface has a much higher surface energy than ZnO $(10\bar{1}0)$, but it is still slightly lower in energy than the other nonpolar surface, $(11\bar{2}0)$, of GaN[49]. Experimentally, the $(10\bar{1}0)$ surface of GaN often appears as the inside wall of nanopipe defects[9–13]. These considerations all suggest that $(10\bar{1}0)$ is at least one of the most stable GaN surfaces.

3.2 Calculation

We use a density functional theory (DFT) approach to study the adsorption structures and energetics. Our model system is a 5 double-layer GaN slab built from wurtzite GaN with exposed $(10\bar{1}0)$ surfaces. H_2O molecules are adsorbed on both sides. The slabs in adjacent supercells are separated by a vacuum layer of at least 9 Å. We consider both full (1 ML) coverage, in which each unit cell of the GaN $(10\bar{1}0)$ surface has an H_2O adsorbed, and partial (1/4 ML) coverage. The in-plane lattice parameters of the slab are set to the corresponding GaN bulk lattice parameters a and c, and the middle double-layer is fixed to its bulk

position during relaxations. We use the plane-wave pseudopotential method, coded in the Quantum Espresso/ PWSCF package[50], with Vanderbilt ultrasoft pseudopotentials[51]. The Perdew-Burke-Ernzerhof (PBE)[22] version of the generalized gradient approximation (GGA) exchange-correlation functional is employed. The Ga 4s, 4p, and 3d states, N 2p and 2s states, and O 2p and 2s states are explicitly treated as valence electrons with a plane-wave expansion for the basis set. The calculated results for bulk GaN and molecular water agree with experiments[52–61] and previous calculations[62–66] (see the Supporting Information). Selected testing with GaN slabs up to 10 double layers thick indicates that the bare surface energy is converged with 5 double layers to about 0.05 eV/f.u. and water adsorption energies to about 0.001 eV per H_2O. The energy barriers for H_2O molecule dissociation are computed using the nudged elastic band (NEB) method[67, 68]. Further details are given in the Supporting Information.

3.3 Results

3.3.1 Bare Surface

First, the structure of the bare wurtzite $(10\bar{1}0)$ surface of GaN is computed (see Table 3.1). The results agree with a previous calculation using the local density approximation (LDA)[49], but we find a lower surface energy due to our use of the GGA. The surface energy of GaN is much higher (>1 eV/f.u.) than that of ZnO[48, 49]. The tilting angle of the surface Ga-N bond is smaller than that of the Zn-O bond. Both results confirm that the Ga-N bond is more

Table 3.1: Comparison of surface energy (E_{surf}), tilting angle of surface anion-cation cond (ω), and surface bond contraction (BC) for our bare surface results (GGA) and previous LDA calculations[a]

	GaN GGA	GaN LDA	ZnO GGA	ZnO LDA
E_{surf}(eV/f.u.)	1.60	1.95	0.5	0.8
$\omega(^\circ)$	8.2	7	10.1	10.7
BC(%)	7.4	6	7.2	6.7

[a] Results for ZnO are also listed. The surface energy Esurf equals the total energy of a relaxed slab minus the total energy of bulk with the same number of atoms, per formula unit (f.u.) of surface atoms, each formula unit consisting of a cation-anion pair.

covalent than the Zn-O bond. The surface N is not fully coordinated, having a vacant coordination site owing to a missing Ga atom. This vacant site is not passivated well by the electrons of the three neighboring Ga atoms. The surface energy for one f.u. of surface GaN is similar to 1/4 of the cohesive energy of bulk GaN, i.e., the energy of one Ga-N bond[49, 54]. In the ZnO case, the crystal is more ionic and the vacant coordination site of the more electronegative O atom is better passivated by electrons of neighboring Zn atoms, resulting in a much smaller surface energy.

3.3.2 Water Adsorption Geometry

For full monolayer coverage ($\theta = 1$), there is one H_2O molecule in each surface area unit, which contains a pair of atoms, one Ga and one N. We relax the lattices for 7 adsorption geometries (see Figures 3.1 and 3.2): Two cases are dissociative adsorption (Dis1 and Dis2) and four cases are molecular adsorption

(Mo1-Mo4). We also consider the (2×1) halfdissociation (HD) described further below. Results are shown in Table 3.2 including comparison to previous results for ZnO. The adsorption energy $E_{\text{ad}} = E_{\text{slab}} + E_{\text{water}} - E_{\text{total}}$ is the energy released from water adsorption, where Eslab is the total energy of the relaxed bare slab and Ewater is the total energy of a relaxed water molecule. Under the constraint of (1×1) periodicity, the dissociative adsorption geometry Dis1 is found to be energetically the most stable. It is 1.44 eV lower in energy than the corresponding (and most stable) molecular adsorption geometry Mo1. This result shows a strong tendency for water to dissociate on this surface. The Mo4 structure, stable on ZnO under the (1×1) constraint[14], is found to be unstable on GaN. Any starting configuration near it will relax into Dis1.

When the (1×1) restriction is lifted, a monolayer of water on the ZnO $(10\bar{1}0)$ surface forms a half-dissociated (2×1) superstructure: a mixture of Dis1 and Mo4.3a We also tested this half-dissociation (HD) configuration for GaN. In this case, a 1.72 Å hydrogen bond is formed between the adjacent H_2O and OH groups, as shown in Figure 3.1c. This stabilizes half of the cell in the Mo4 geometry and makes HD the second most stable configuration. However, this configuration is still higher in energy than total dissociative adsorption Dis1. For completeness, we consider Mo2, a rotated version of Mo1, as well as an alternative dissociative adsorption, Dis2, along with its molecular adsorption analogue, Mo3. None of these structures turn out to be energetically competitive with Dis1. We believe that the ground-state of a water monolayer on GaN $(10\bar{1}0)$ is the completely dissociative state Dis1. The key difference compared to ZnO is the more covalent nature of the Ga-N bond. The surface N atom retains strong dangling-bond character and will readily

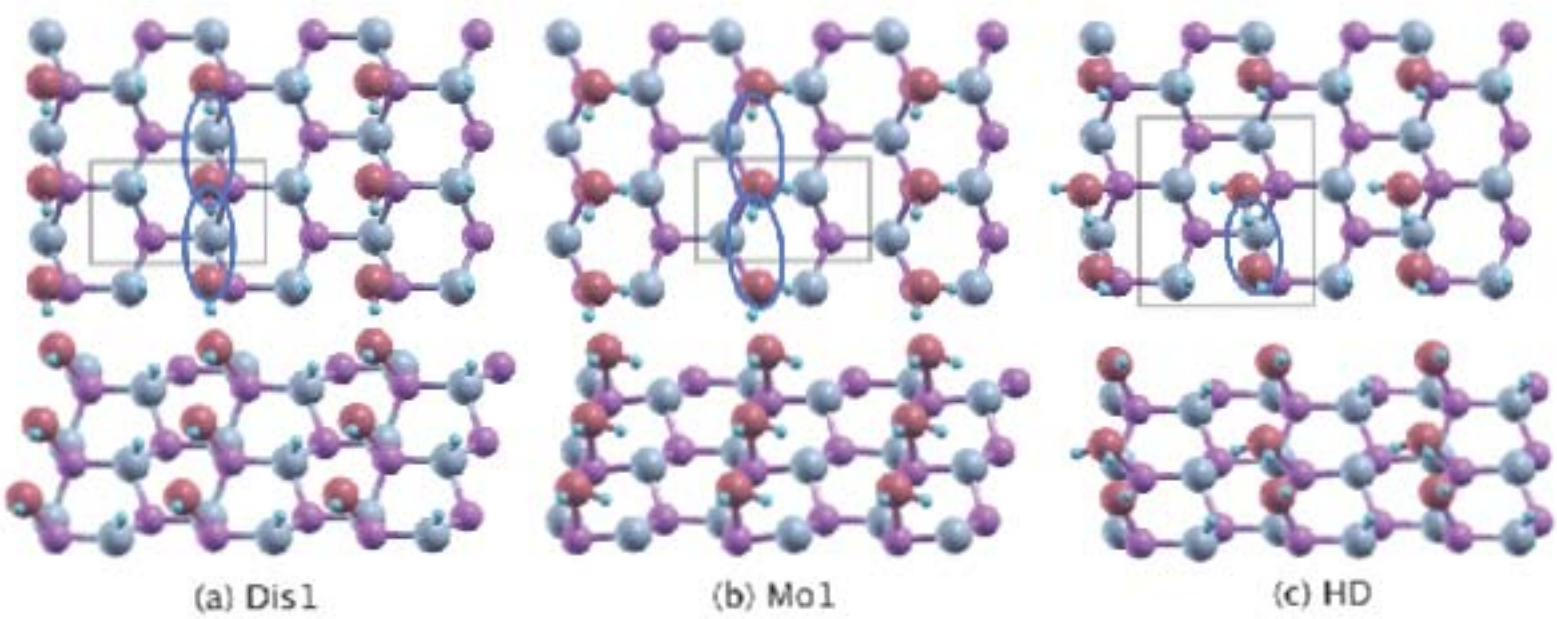

Figure 3.1: Water adsorption geometries: (a) dissociative adsorption 1 (Dis1); (b) molecular adsorption 1 (Mo1); (c) half-dissociation (HD). Ga is in purple, N is in gray, O is in red, and H is in blue. The blue circles show key H-bond interactions. The gray boxes show the (1×1) and (2×1) unit cells.

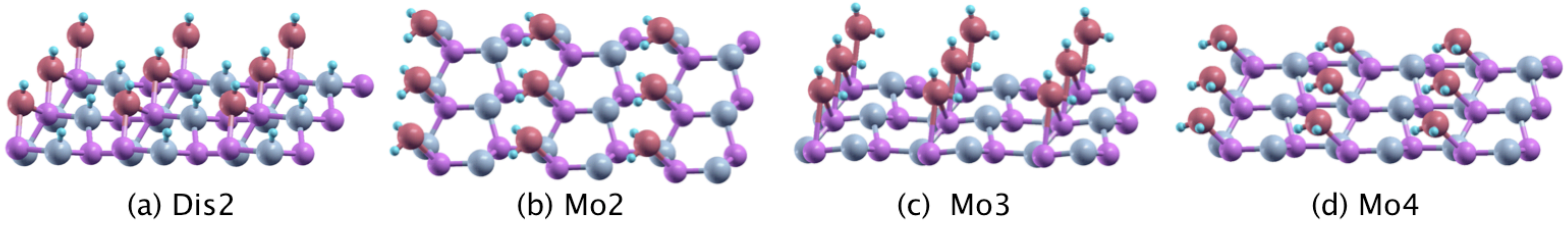

Figure 3.2: Water adsorption geometries: (a) dissociative adsorption 2 (Dis2); (b) molecular adsorption 2 (Mo2); (c) molecular adsorption 3 (Mo3); (d) molecular adsorption 4 (Mo4).

Table 3.2: Water adsorption energy E_{ad}(eV) on the wurtzite $(10\bar{1}0)$ surface: comparison between GaN and ZnO

	GaN ($\theta = 1$)	GaN ($\theta = 1/4$)	ZnO ($\theta = 1$)[14]	ZnO ($\theta = 1/6$)[45]
Dis1	2.18	1.71		0.63
Dis2	1.65	1.37		0.79
Mo1	0.74	0.68		0.57
Mo2	0.50	0.72		0.61
Mo3	0.26	0.43[b]		0.42
Mo4	*a*	*a*	1.03	0.94
HD	1.83	n.a.	1.13	

[a] Unstable to dissociation.

[b] For $\theta = 1/4$, since these structures can easily relax to dissociated configurations, they may not be proper potential energy minima. Relaxations were stopped when forces were smaller than 0.03 eV/Å.

react to fill its vacant coordination site to reduce the surface free energy.

3.3.3 Barrier for Dissociation

The Mo1 and HD configurations appear to be local minimumenergy structures. We used the NEB method to determine the energy barriers for dissociation. For Mo1 transforming to Dis1, we obtain an energy barrier of 1.0 meV (Figure 3.3). For HD transforming to Dis1, we obtain an energy barrier of 1.6 meV. The absolute values of such small energy barriers lie below the accuracy of DFT methods. Nevertheless, the DFT results indicate that the barriers are

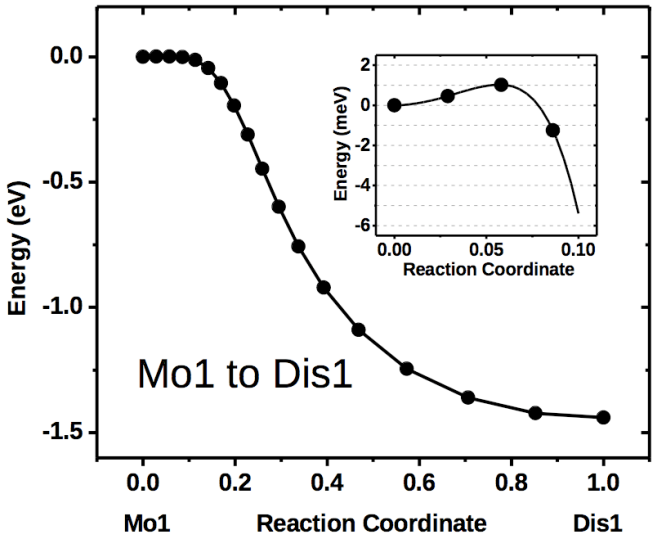

Figure 3.3: Minimum energy path (MEP) for a full monolayer of water to dissociate from Mo1 to Dis1. The inset is a blown-up view of the dissociation barrier. The points are the energies of NEB images, and the lines are cubic interpolations of the energy along the MEP. The MEP corresponds to dissociation on one side of the slab while the water adsorbed on the other side remains in a molecular configuration. The slab is sufficiently thick so that there is essentially no interaction between the surfaces.

small relative to the thermal energy, k_BT, at room temperature ($\sim$ 26 meV). Therefore we expect a full monolayer of water to dissociate spontaneously at room temperature.

3.3.4 Adsorbates Interaction

Will water aggregate into islands at submonolayer coverage? To probe the effective adsorbate interactions, we also compute the case of a 1/4 ML coverage ($\theta = 1/4$) of water, where the periodicity in both the a and c axes is doubled, and each (2×2) surface cell contains only one water molecule. For the dissociative adsorptions, we only consider the case where the O-H group and

H are in the same (1×1) surface cell. At this coverage, the water molecules can be viewed as approximately isolated. The Dis1 geometry is still the most stable, but the adsorption energy is reduced by 0.47 eV/(f.u. of H_2O). The adsorption energy for Dis2 is reduced by a smaller amount, 0.28 eV/f.u., but Dis1 remains the lowest energy structure. Smaller changes are seen for the molecular adsorption cases. Overall, the results clearly indicate that dissociative adsorption is still favored at low coverage, and that there is a substantial energetic driving force toward aggregation. There are two kinds of adsorbate interactions driving aggregation, direct and strain induced.

To better understand the adsorbate interactions, we decompose the molecular adsorption energy into several contributions, similar to ref [45]. We write, for coverage θ

$$E_{\mathrm{ad}}(\theta) = E^0_{\mathrm{WS}}(\theta) - \delta E_{\mathrm{W}}(\theta) - \delta E_{\mathrm{S}}(\theta) + E_{\mathrm{WW}}(\theta)$$

Here E^0_{WS} is the adsorption energy if we strain the (isolated) water molecules and the substrate to their final adsorbed geometries before putting them together, δE_{W} is the energy required to distort the water molecule, δE_{S} is the energy required to distort the substrate, and the E_{WW} term is the increase in E_{ad} due to direct water-water interactions. The substrate strain term, δE_{S}, is calculated by eliminating the water molecules from the slab while fixing the GaN substrate atoms in their wateradsorbed geometry and comparing to the relaxed slab: $\delta E_{\mathrm{S}} = E_{\mathrm{strained}}(\mathrm{GaN}) - E_{\mathrm{relaxed}}(\mathrm{GaN})$. The water molecule distortion energy is calculated in an analogous way. The direct water-water interaction E_{WW} is calculated by eliminating the substrate and fixing the water

molecules at the adsorbed geometry to calculate the energy per water molecule E_{W1}. Then the separation between water molecules is increased to 10 Å, still fixing the internal coordinates of water molecules, and the isolated water energy E_{W2} is calculated. Finally, $E_{\mathrm{WW}} = E_{\mathrm{W2}} - E_{\mathrm{W1}}$. The results are shown in Table 3.3.

We find that δE_{S} is small but coverage dependent for molecular adsorption; it is smaller at higher coverage. This indicates that close-neighbor adsorbates have an effective attractive interaction attributable to sharing the substrate strain. On the other hand, the direct water-water interaction depends on the structure. For the energetically favored molecular adsorption case, Mo1, E_{WW} is positive; water molecules attract each other, increasing the total adsorption energy. For Mo2 and Mo3, the E_{WW} terms are negative, indicating repulsion. The attractive interaction in Mo1 comes from the formation of hydrogen bonds between neighboring (1×1) cells (see Figure 3.1b).

For dissociative adsorption, the charge distributions around O and H can differ between the adsorbed state and detached state, so the above method to isolate E_{WW} is no longer directly applicable. However, the substrate strain term can be evaluated in the same way. For dissociative adsorptions, we only analyze the substrate strain term, without further decomposing the total adsorption energy. As seen in Table 3.3, the magnitude of δE_{S} is substantially larger. Also the effective attraction due to shared strain is larger than in the molecular adsorption cases. Furthermore, the shared strain effect is larger for Dis2 (0.45 eV/f.u.) than for Dis1 (0.15 eV/f.u.). Other interactions are also important. For Dis2, the total effective attraction from Table 3.2 (0.28 eV/f.u.) is about half of the attraction due to shared strain. On the other hand,

Table 3.3: Analysis of the contribution of strain energy and direct water-water interactions in the water adsorption energies (in units of eV per H_2O molecule; see text)

	$E^0_{\mathrm{WS}}(\theta = 1/4)$	$E^0_{\mathrm{WS}}(\theta = 1)$	$\delta E_{\mathrm{W}}(\theta = 1/4)$	$\delta E_{\mathrm{W}}(\theta = 1)$	$\delta E_{\mathrm{S}}(\theta = 1/4)$	$\delta E_{\mathrm{S}}(\theta = 1)$	$E_{\mathrm{WW}}(\theta)$
Dis1					0.79	0.64	
Dis2					1.34	0.89	
Mo1	0.78	0.77	0.05	0.14	0.06	0.06	0.17
Mo2	0.86	0.79	0.02	0.10	0.12	0.09	-0.11
Mo3	0.49	0.36	0.01	0.11	0.04	0.03	-0.06

for Dis1 the total effective attraction (0.47 eV/f.u.) is more than triple the substrate strain effect. While it is not possible to clearly define and separate the terms E^0_{WS} and δE_{W} in the case of dissociative adsorption, it is clear that δE_{W} is quite large (an OH bond is broken) and E^0_{WS} is correspondingly large to compensate for the water distortion energy. For Dis1, it is clear that hydrogen bonds form between neighboring (1×1) cells (Figure 3.1a). Thus, for the energetically favored dissociative (Dis1) adsorption configuration, the hydrogen bonding stabilizes the dense layer. In the true ground-state Dis1, this direct adsorbate attraction by hydrogen bonding, together with the indirect attraction by sharing the strain and the compensation between E^0_{WS} and δE_{W} will drive the adsorbates toward aggregation in submonolayer coverage.

3.4 Summary

In summary, we have studied the adsorption energy of H_2O molecules on a wurtzite $(10\bar{1}0)$ GaN surface for full and 1/4 monolayer coverages, and calculated the energy barrier for water dissociation. Water is found to adsorb dissociatively, and the dissociation barrier is negligible. We also examined the effect of substrate strain and hydrogen bonding. Both effects favor the aggregation of dissociated water molecules into islands under submonolayer coverage.

3.5 Supporting Information

3.5.1 Theoretical Procedures

The planewave basis set used is determined by a kinetic energy cutoff of 30 Ry for the Kohn-Sham orbitals and 400 Ry for the charge density. The bulk wurtzite Brillouin zone is sampled using a 10x10x10 k-point mesh. A 4x1x2 k-point mesh is used for (1x1) surface calculations, and a 2x1x1 k-point mesh is used for (2x2) supercell calculations. The geometry is optimized using the Broyden-Fletcher-Goldfarb-Shanno (BFGS) method[69]. During the relaxation, a Gaussian broadening[70] with smearing parameter of 0.002 Ry is used for Brillouin-zone integrations to prevent possible convergence problems due to fractionally occupied surface states. The force on each movable atom is converged at 0.003 eV/Å, except where explicitly noted. Using a 4x4x2 k-point mesh gives an error smaller than 10 meV/f.u. in the total energy, and the errors in the lattice parameters are smaller than 0.1%. This justifies our use of 4x1x2 k-point mesh for the (1x1) slab calculations. The bulk cohesive energy is obtained by subtraction of the total energy per GaN formula unit at the equilibrium position, from the sum of the energy of isolated Ga and N atoms, with spin-polarization, but not including the zero-point motion. The isolated atom energies are calculated by arranging each atom on a simple cubic supercell with lattice parameter 11 Å. The bulk modulus is obtained by fitting the total energy as a function of volume to the Murnaghan equation of state[71]. For reference, the computed structural and cohesive properties of the bulk wurtzite phase GaN are shown in Table 3.4. Our results agree well with other GGA calculations[62, 63] and with experiments to the expected

Table 3.4: Comparison between our bulk results and other GGA calculations and experiments.[a]

	This Work	GGA I[62]	GGA II[63]	Exp.
a(Å)	3.219	3.245	3.1986	3.190[52], 3.1890[53]
c/a	1.629	1.632	1.6339	1.627[52], 1.6265[53]
u	0.377	0.3762	0.3772	0.377[52]
E_{coh}(eV/f.u.)	8.57	8.265	9.265	9.0[54]
B_0(Mbar)	1.72	1.72		1.88-2.45[55–58]
B'	4.1	5.11		3.2-4.3
B_g(eV)	1.69	1.45		3.41[59]

[a] The spacing between closest Ga and N layers is $(1/2 - u)c$.

tolerance[52–59].

The energy barriers for H_2O molecule dissociation are computed using the nudged elastic band (NEB) method[67] employing 18 images connected by a spring with variable spring constant[68] between 0.1 and 0.6 a.u.. The climbing image scheme[68] is used to find the saddle point. The path is converged to 0.02 eV/Å.

The energy of a single H_2O molecule is calculated by relaxing an isolated H_2O molecule in a cubic supercell with lattice parameter 14 Å. Our O-H bond length, H-O-H bond angle, and total electric dipole moment are in good agreement with other DFT calculations and experiments (see Table 3.5).

Since the adsorption energy for molecular H_2O adsorption is found to be modest scale in our GGA calculations, the absence of van der Waals terms may be a significant source of error. The H_2O molecule is attached to the

Table 3.5: Comparison of O-H bond length r, $\angle$HOH bond angle θ, and dipole moment d between our water molecule results and other DFT calculations and experiments.

	This Work	GGA (BLYP)[64]	GGA (PBE)[65]	GGA (BLYP)[66]	Exp.
r(Å)	0.975	0.973	0.970	0.967-0.974	0.957[60]
θ(°)	104.4	104.4	104.2	104.0-104.4	104.5[60]
d(a.u.)	1.83	1.81	1.81	1.89-2.13	1.85[61]

surface Ga atom. The van der Waals interaction energy U between the Ga atom and the H_2O molecule can be expressed as $U = -C/r^6$. The constant C can be estimated from the Hamaker constant A by the relation $C = A/(\pi^2\rho_{\text{water}}\rho_{\text{Ga}})$[72]. The Hamaker constant between Ga and water can be estimated by the Berthelot approximation $A = \sqrt{A_{\text{water}}A_{\text{Ga}}}$[73]. We use the value $A_{\text{Ga}} = 2.7\times10^{-21}$ J (the Hamaker constant of α-Ga, averaged over 3 faces)[74] and $A_{\text{water}} = 4.0\times10^{-20}$ J[75]. In Mo1, the Ga-O distance r is 2.2 Å, and we obtain $U \sim -0.03$ eV (the negative sign means attractive interaction). The van der Waals interaction in Mo2 and Mo3 should be similar or weaker, so the van der Waals interaction source of DFT error does not seem important in this problem.

As mentioned in the main text, the energy to strain the substrate, δE_{S}, is smaller for molecular adsorptions. Table 3.6 shows the thicknesses of the GaN substrates under full coverage. It shows that the distortion is indeed larger in dissociative adsorptions and smaller in molecular adsorptions.

Table 3.6: Thicknesses of the GaN substrates under full coverage and bare slab results.[a,b,c,d]

	Thickness(Å)	Expansion(Å)
Bare slab unrelaxed	12.08	0.27
Bare slab relaxed	11.81	0
Dis1	12.06	0.25
Dis2	12.19	0.38
Mo1	11.86	0.06
Mo2	11.96	0.16
Mo3	11.88	0.07

[a] The thicknesses are measured from the centers of the tilting surface Ga-N bonds on both sides of the model slab.

[b] The relaxed bare slab is used as a reference to calculate the expansions.

[c] Compared with fresh cut unrelaxed slab, the relaxed slab contracts inward.

[d] When H_2O molecules adsorb, the GaN substrate will be distorted outwards, showing a positive expansion.

3.6 Afterword

So far Chapter 3 is a verbatim copy of J. Phys. Chem. C vol. 113, p. 3365-3368. This section adds a few words. In this paper, we have observed that the ground state of a monolayer of dissociated water (in the form of hydroxide ions attached to surface Ga atoms forms a hydrogen bond network parallel to the $(10\bar{1}0)$ wurtzite surface, with O-H bonds pointing towards neighbor hydroxide ions at the surface, along the (0100) direction. Recently, our colleague Jue Wang, under the supervision of Prof. Maria V. Fernandez-Serra, has studied the interface between the same GaN $(10\bar{1}0)$ surface and bulk water by first-principles molecular dynamics. His results confirm our finding of water dissociation, but also indicate that that the hydrogen bond network parallel to the surface will be disrupted in the presence of bulk water He found that the hydroxide ions attached to surface Ga are more likely to form hydrogen bonds with the water molecules in bulk water, with O-H bonds pointing towards the O atoms in the bulk water molecules.

Chapter 4

Water Oxidation on GaN $(10\bar{1}0)$ surface

4.1 Introduction

Both GaN and ZnO are wide band-gap semiconductors that absorb only UV light. In 2005, a solid solution of GaN and ZnO was synthesized by Domen's group. This solid solution has a narrowed band gap and can absorb visible light. When small nanoparticles of a co-catalys for proton-reduction are loaded onto larger nanoparticles of the solid solution, the assembly can photo-split water into H_2 and O_2[1]. The co-catalyst reduces protons to H_2 with the photo-electrons. The surface of the solid solution oxidizes water into O_2 plus protons using the photo-holes. The highest achieved quantum efficiency of overall water splitting was 5.9% when the wave length of incident light was between 420 and 440 nm[6]. When the proton reduction reaction was short-circuited by using Ag^+ as a sacrificial reagent for scavenging electrons, the quantum

efficiency for oxidizing water into O_2 reached 51%[3]. This shows that the surface of the solid solution photo-catalyst itself is also a good catalyst for water oxidation, making it a good candidate for the photo-anode in a photo-elecrochemical cell for solar water splitting[7]. Understanding the details of the water oxidation mechanism at this semiconductor alloy/aqueous solution interface, and why the quantum efficiency so high, would provide valuable information for the discovery and design of new materials for semiconductor photocatalysts and photo-anodes for solar water splitting.

Pure GaN itself also works as an overall water splitting catalyst in the UV region when loaded with a suitable co-catalyst, and has a quantum efficiency 0.7% at 300 - 340 nm[8]. When the proton reduction half-reaction is short-circuited, the quantum efficiency for O_2 also increase significantly on pure GaN without a co-catalyst. It is unclear on which surface the oxidation occurs. Our previous study of water adsorption on the GaN $(10\bar{1}0)$ surface has shown that a monolayer of water will dissociate completely on that surface, with the proton attaching to a surface N atom and the hydroxide ion attaching to a surface Ga atom[15]. This paper presents computational evidence for a possible water oxidation mechanism on that surface.

4.2 Method

The reaction mechanism for water oxidation on a TiO_2 surface was studied by Valdes et al.[76]. The semiconductor/aqueous interface was modeled by a slab with a monolayer of adsorbed intermediates. No solvent effects were included. The calculations were carried out using a periodic code for density

functional theory (DFT) with a generalized gradient approximation (GGA). In this paper, we attempt to construct and explore a more realistic model. The semiconductor/aqueous interface is represented by a fragment of the wet surface. The computations are done with a cluster code, which enables us to use the a hybrid density functional[26] at moderate computational cost, and describe the solvent effects by the combination of explicit solvent molecules and a polarizable continuum model. This approach is expected to yield better energetics than the DFT-GGA calculations without solvent.

As illustrated in Fig. 4.1, we cut a fragment of the water-coated GaN surface, obtaining a cluster which incorporates a (2×1) unit of the primitive $(10\bar{1}0)$ surface cell. The surface Ga atom in one of the two unit cells is considered to be the active site. Initially, this site is occupied by a hydroxide ion. Our model also includes explicit water molecules. Four additional water molecules are added in the initial configuration: two of them will become reactant water molecules, and the other two are used to solvate the active site and the attached intermediates. The dangling bonds formed by cutting the cluster are passivated. The N dangling bonds are passivated by hydrogen atoms, and the Ga dangling bonds are passivated by fluorine atoms. The choice of fluorine atoms was motivated by the criterion of having the valence orbitals of the passivating atom well below the frontier orbitals, but the electronegative fluorine atoms may spuriously influence the electron density at the active Ga site.

All computations were carried out using hybrid density functional theory with the Gaussian03 code[77]. The D95V basis set[30] was used for the H, O, F atoms. The valence and core electrons of Ga atoms were described by

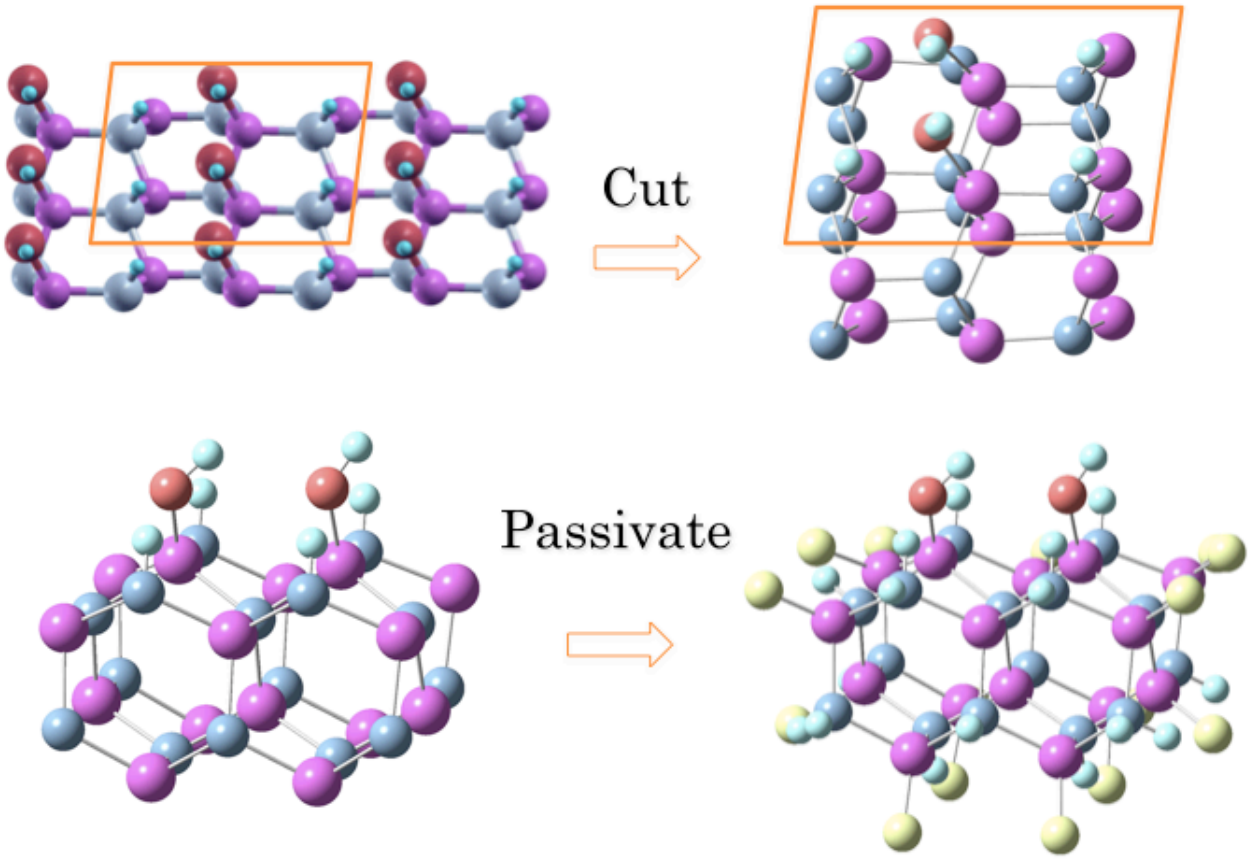

Figure 4.1: Construction of the cluster. The orange box denotes an (2x1) unit cell of water adsorbed $(10\bar{1}0)$ surface of wurtzite GaN. Ga is in purple, N is in grey, O is in red, H is in blue, and F is in yellow.

the LANL2DZ basis and effective core potential (ECP), respectively[78–80], with the 3d electrons included in the core. This combination is denoted as the LANL2DZ basis set in Gaussian. The B3LYP hybrid functional[21, 23, 24, 27] was employed. In addition to the explicit water molecules, an implicit solvent model (condutor-like screening model, or COSMO)[32] was used to describe the extended aqueous environment. The united topological model, optimized for density functional theory[42], was used to construct the cavity for the cluster in the dielectric continuum. This option is denoted as "CPCM with UAKS radii" in the Gaussian code. The geometries of the cluster plus explicit water molecules were relaxed with the implicit solvant model. Vibrational frequencies were calculated at the relaxed geometry with the implicit solvent, and the Gibbs free energy, including the zero-point, thermal corrections and entropy) was calculated.

4.3 Results

4.3.1 Reference Potential

The absolute potential of normal hydrogen electrode (NHE) is calculated as following: $E^{\circ}_{\mathrm{NHE}} = -\Delta G^{*}_{\mathrm{NHE}}/F$, where $\Delta G^{*}_{\mathrm{NHE}} = G^{*}_{\mathrm{s}}(\mathrm{H}^{+}) + G^{\circ}_{\mathrm{g}}(\mathrm{e}^{-}) - G^{\circ}_{\mathrm{g}}(\mathrm{H}_2)/2$ is the change of free energy for the one-electron hydrogen oxidation reaction at the normal hydrogen electrode, and F is the Faraday constant which equals 1 when we use eV for free energy and Volts for potential. Here $G^{\circ}_{\mathrm{g}}(\mathrm{H}_2)$ is the standard state free energy of a gas-phase H_2 molecule, whose value is taken from our B3LYP/D95V calculations. (We use G°_{g} to denote a free energy

in the standard state in the gas phase. Similarly, G^*_s denotes a free energy in the standard state of 1 molar in aqueous solution.) $G^o_g(e^-)$ is the free energy of a gas-phase electron. At 298 K, $G^o_g(e^-) = -0.006$ kcal/mol, and is consequently neglected in our calculations. The standard state free energy of a proton in aqueous solution, $G^*_s(H^+)$, is calculated as $G^o_g(H^+) + \Delta G^o_s(H^+)$, where $G^o_g(H^+) = -0.27$ eV (-6.28 kcal/mol) is the free energy of the gas-phase proton derived from Sackur-Tetrode equation[43], $\Delta G^o_s(H^+) = -11.45$ eV (-263.98 kcal/mol) is the solvation energy of proton, using the standard concentration of 1 bar in gas phase and 1 mol/L in the aqueous phase[81]. We obtain $G^*_s(H^+) = -270.26$ kcal/mol $= -11.72$ eV so that $\Delta G^*_{NHE} = 4.28$ eV, and $E^o_{NHE} = -4.28$ V.

The "theoretical" standard reduction potential (i.e., the standard reduction potential obtained using our choices of the density functional, the basis set, and the solvent model), for the four-electron oxygen reduction reaction, $E^o(O_2 + 4H^+ + 4e^- \rightarrow 2H_2O)$, is calculated as: $E^o(O_2 + 4H^+ + 4e^- \rightarrow 2H_2O) = -\Delta G^*(O_2 + 4H^+ + 4e^- \rightarrow 2H_2O)/4F = -(2G^*_s(H_2O) - 4G^*_s(H^+) - G^o_g(O_2) - 4G^*_{NHE})/4F$, where $G^*_s(H_2O)$ is the free energy of water molecule in aqueous standard state, and $G^o_g(O_2)$ is the free energy of a triplet O_2 molecule in the gas-phase standard state. The values of $G^*_s(H_2O)$ and $G^o_g(O_2)$ are taken from our B3LYP/LANL2DZ calculation. We obtain $\Delta G^*(O_2 + 4H^+ + 4e^- \rightarrow 2H_2O) = -4.55$ eV, and $E^o(O_2 + 4H^+ + 4e^-/2H_2O) = 1.14$ V. The experimental oxygen reduction potential is 1.23V.

4.3.2 Key Intermediates

We begin by defining several terms. As mentioned before, we will use the term "cluster" to describe the group of atoms containing the fragment of the surface with the attached reactive intermediates. We will use the term "model" to describe the "cluster" plus explicit solvent water molecules. We will use the term "system" to describe the "model" plus the products such as the O_2 molecule, protons and electrons. We denote the initial cluster (Fig. 4.1, lower right) as $*OH^-$. The * is the surface Ga site, and $*OH^-$ means that this surface Ga site is occupied by a hydroxide ion, OH^-. In our cluster, * can be interpreted as a molecular group with the formula $(Ga_{15}N_{15}F_{15}O_1H_{18})^+$. To search for possible intermediates, we remove electrons from the cluster sequentially (and remove protons at the same time) to simulate a proton-coupled oxidation process at each step of the reaction mechanism. These calculations are done in the gas phase. We find intermediates $*O^{\bullet-}$, $*OOH^-$, and $*O_2^{\bullet-}$ after removing 1, 2 and 3 electrons. The assignments of $*O^{\bullet-}$ and $*O_2^{\bullet-}$ as radical ions were confirmed by spin-density analysis. When we remove the fourth electron, the $*O_2^{\bullet-}$ is oxidized into an O_2 molecule, which detaches from the cluster. In order to calculate the energies of these intermediates in the aqueous phase, the corresponding cluster models are relaxed with explicit solvent water molecules and a polarizable continuum. Reactant water molecules are also included explicitly.

The clusters corresponding to the key intermediates with explicit water molecules are shown in Fig. 4.2 as model (a), (b), (c), (d) and (a′). Model (a) can be expressed as $*OH^-\cdot(H_2O)_4$, (b) as $*O^{\bullet-}\cdot(H_2O)_4$, (c) as $*OOH^-\cdot(H_2O)_3$,

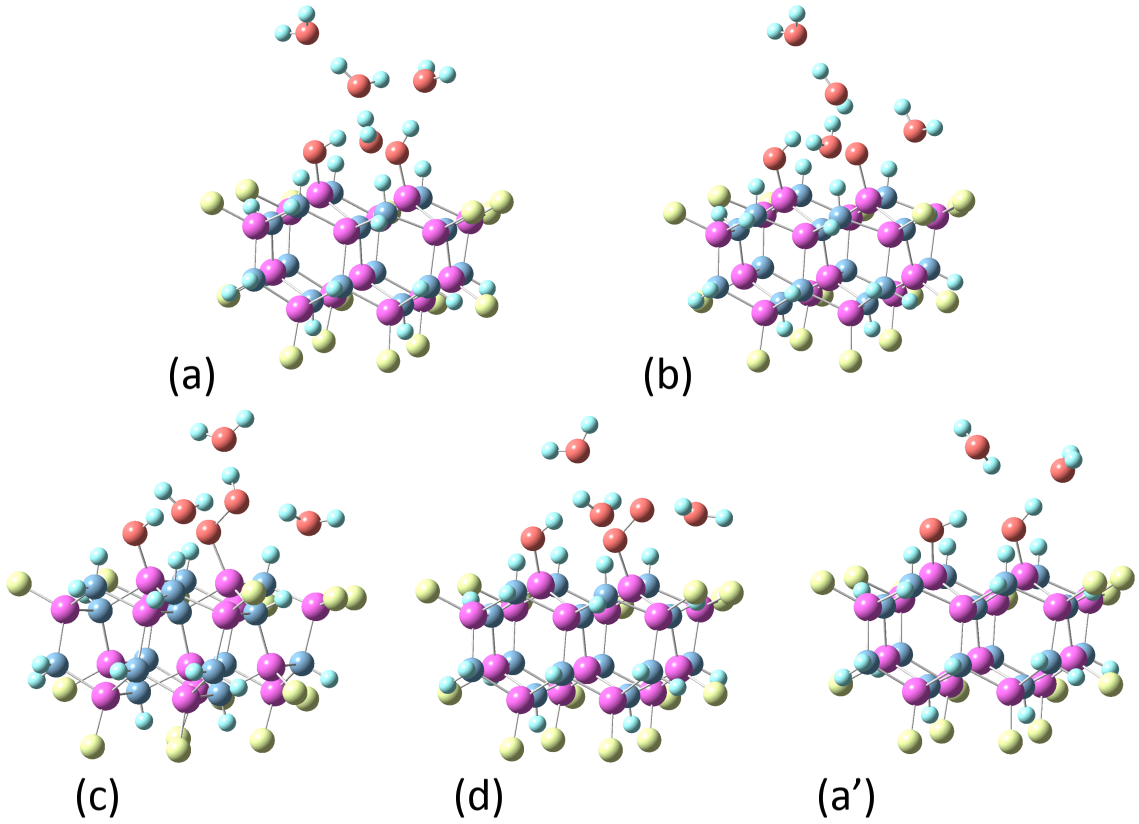

Figure 4.2: Relaxed structures for the models of intermediates: (a) $^*OH^- \cdot (H_2O)_4$, (b) $^*O^{\bullet -} \cdot (H_2O)_4$, (c) $^*OOH^- \cdot (H_2O)_3$, (d) $^*O_2^{\bullet -} \cdot (H_2O)_3$, and (a′) $^*OH^- \cdot (H_2O)_2$.

Table 4.1: Change of free energy in the reactions

	ΔG(abs)(eV)	ΔG(eV)
$^*OH^- \rightarrow {}^*O^{\bullet -} + e^- + H^+$	7.09	2.81
$^*O^{\bullet -} + H_2O \rightarrow {}^*OOH^- + e^- + H^+$	5.31	1.03
$^*OOH^- \rightarrow {}^*O_2^{\bullet -} + e^- + H^+$	5.92	1.64
$^*O_2^{\bullet -} + H_2O \rightarrow {}^*OH^- + O_2 + e^- + H^+$	3.53	-0.74

(d) as $^*O_2^{\bullet -}\cdot(H_2O)_3$, and (a′) as $^*OH^-\cdot(H_2O)_2$. All these models are charge neutral when taken together with the corresponding hole (h^+). Models (a), (c) and (a′) are singlets, and models (b) and (d) are doublets. Their free energies $G_s^*(i)$ (i=a, b, c, d, and a′), are calculated at the relaxed geometries, which are shown in Fig. 4.2.

4.3.3 Reaction Pathway

The intermediates are connected by 4 steps of proton-coupled electron-transfer (PCET) reactions, written as follows:

(1) $^*OH^- \rightarrow {}^*O^{\bullet -} + e^- + H^+$

(2) $^*O^{\bullet -} + H_2O \rightarrow {}^*OOH^- + e^- + H^+$

(3) $^*OOH^- \rightarrow {}^*O_2^{\bullet -} + e^- + H^+$

(4) $^*O_2^{\bullet -} + H_2O \rightarrow {}^*OH^- + O_2 + e^- + H^+$

The absolute changes of free energy in each step of the reaction are calculated as:

(1) a $\rightarrow$ b + e^- + H^+,

$$\Delta G_1(\text{abs}) = G_s^*(\text{b}) + G_s^*(\text{H}^+) - G_s^*(\text{a})$$

(2) $\text{b} \rightarrow \text{c} + \text{e}^- + \text{H}^+$,

$$\Delta G_2(\text{abs}) = G_s^*(\text{c}) + G_s^*(\text{H}^+) - G_s^*(\text{b})$$

(3) $\text{c} \rightarrow \text{d} + \text{e}^- + \text{H}^+$,

$$\Delta G_3(\text{abs}) = G_s^*(\text{d}) + G_s^*(\text{H}^+) - G_s^*(\text{c})$$

(4) $\text{d} \rightarrow \text{a}' + \text{O}_2 + \text{e}^- + \text{H}^+$,

$$\Delta G_4(\text{abs}) = G_s^*(\text{a}') + G_g^{\text{o}}(\text{O}_2) + G_s^*(\text{H}^+) - G_s^*(\text{d})$$

The change of free energy relative to NHE, $\Delta G_i(i{=}1,\ 2,\ 3,\ 4)$, is equal to $\Delta G_i(\text{abs}) - 4.28$ eV. The $\Delta G_i(\text{abs})$ and ΔG_i for each step of reaction are listed in Table 4.1. The most difficult step, i.e., the step that has the highest change in free energy, is the first step (a $\rightarrow$ b), in which the adsorbed hydroxide ion OH^- loses one electron and one proton, and becomes an adsorbed $\text{O}^{\bullet-}$ radical. To drive this reaction, a potential of 2.81 V is required. The second most difficult step is the third step (c $\rightarrow$ d), in which the adsorbed hydroperoxide ion OOH^- loses one electron and one proton, and becomes an $\text{O}_2^{\bullet-}$ radical. To drive this reaction, a potential of 1.64 V is required.

Experimental values of the valence band-edge potential of GaN (*vs.* NHE at pH=0) have been reported to be 2.85 V[83], 2.565 V and 3.11 V[84]. This means that the valence band-edge of pure GaN might be sufficient to drive the first step of the reaction. The change of free energy at different electrode potentials U (relative to NHE) along the reaction path is show in Fig. 4.3.

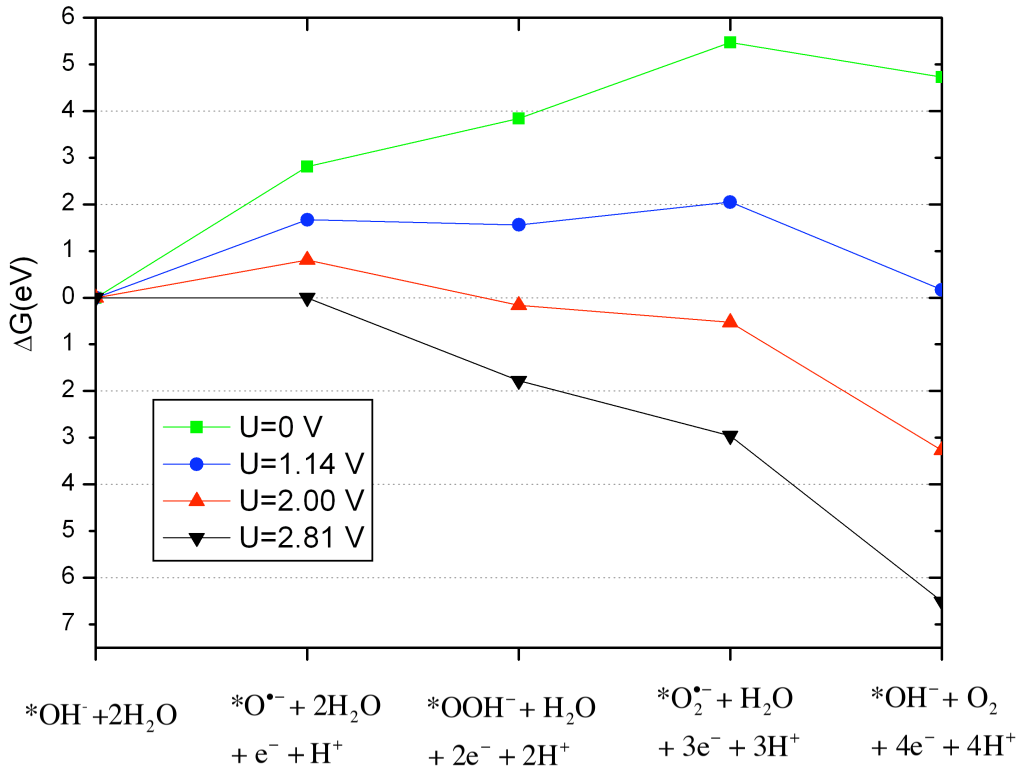

Figure 4.3: The relative free energies of the intermediates along the reaction pathway at pH=0. U is the electrode potential relative to NHE.

Table 4.2: Comparison of standard reduction potentials of reaction on GaN surface and in aqueous solution

Step	On GaN Surface	E^0(V)	In Aqueous Solution	E^0(V)[82]
(1)	$*O^{\bullet -} + e^- + H^+ \rightarrow *OH^-$	2.81	$^{\bullet}OH + e^- + H^+ \rightarrow H_2O$	2.813
(2)	$*OOH^- + e^- + H^+ \rightarrow *O^{\bullet -} + H_2O$	1.03	$H_2O_2 + e^- + H^+ \rightarrow {}^{\bullet}OH + H_2O$	0.714
(3)	$*O_2^{\bullet -} + e^- + H^+ \rightarrow *OOH^-$	1.64	$HO_2^{\bullet} + e^- + H^+ \rightarrow H_2O_2$	1.51
(4)	$*OH^- + O_2(gas) + e^- + H^+ \rightarrow *O_2^{\bullet -} + H_2O$	-0.75	$O_2(gas) + e^- + H^+ \rightarrow HO_2^{\bullet}$	-0.125
(1)+(2)	$*OOH^- + 2e^- + 2H^+ \rightarrow *OH^- + H_2O$	1.92	$H_2O_2 + 2e^- + 2H^+ \rightarrow 2H_2O$	1.763
(3)+(4)	$O_2(gas) + *OH^- + 2e^- + 2H^+ \rightarrow *OOH^- + H_2O$	0.45	$O_2(gas) + 2e^- + 2H^+ \rightarrow H_2O_2 + H_2O$	0.695

The $U = 0$ V (green) line corresponds to NHE. The $U = 1.14$ V (blue) line corresponds to the "theoretical" standard reduction potential for the four-electron water oxidation reaction. The $U = 2.81$ V (black) line corresponds to the required potential of the first reaction, and is close to the valence band-edge potential of pure GaN. Figure 4.3 suggests that all four steps of the photo-oxidation on pure GaN might occur in a "downhill" (i.e. exothermic) fashion. Under the operating condition of a GaN photocatalyst, the first reaction is the rate-limiting step. So far we have considered only one-electron processes. If we allow the two-electron process $^*OH^- + H_2O \rightarrow {}^*OOH^- + 2e^- + 2H^+$ to occur, the standard potential for this two-electron oxidation process would be $\frac{1}{2}(2.81\text{ V}+1.03\text{ V}) = 1.92$V, which is lower than the one-electron oxidation potential for the first reaction.

Both our method and our proposed mechanism are different from those in Ref. [76]. As mentioned before, Ref. [76] does not include any solvent effect, while in our model, the effect of solvent is captured by using a combination of both explicit solvent (water molecules) and implicit solvent (polarizable continuum). We consider our model more realistic in this respect. On the other hand, our model truncates the periodic surface slab, thereby necessitating the passivation of dangling bonds. This is a less realistic treatment of the semiconductor surface. Our proposed mechanism also differs from the mechanisms described in Ref. [76]. In our mechanism, the reaction starts with a hydroxide ion attached the surface Ga site, denoted as $^*OH^-$, and goes through the route $^*OH^- \rightarrow {}^*O^{\bullet -} \rightarrow {}^*OOH^- \rightarrow {}^*O_2^{\bullet -} \rightarrow O_2 + {}^*OH^-$. Our mechanism has no common intermediates and steps with the mechanisms in Ref. [76]. In Ref. [76], one mechanism starts from an undissociated water molecule, and goes

through the route $H_2O + * \rightarrow *OH^{\bullet} \rightarrow *O \rightarrow *OOH^{\bullet} \rightarrow O_2 + *$; the other mechanism starts with an oxygen covered surface site, *O, and goes through the route $*O \rightarrow *OOH^{\bullet} \rightarrow O_2 + * \rightarrow *OH^{\bullet} \rightarrow *O$. Furthermore, unlike the mechanisms in Ref. [76], the stable intermediates in our mechanism do not include a surface vacancy. This is because of our observation that a vacancy Ga site on the GaN $(10\bar{1}0)$ surface is not stable under either of our models of the aqueous environment; it is either occupied by an explicit water molecule (which then will lose a proton) or by the bridging of a neighboring hydroxide ion under a polarizable continuum model.

Our results are obtained for pure GaN. For a GaN/ZnO solid solutions, our result will not apply directly. However, we can use our current result to for pure GaN to illustrate some speculations about the GaN/ZnO solid solution system. For a GaN/ZnO solid solution, the position of the valence band is lower than in pure GaN[85], so there might not be sufficient overpotential to drive the first reaction. The red line shows an example of the free energy profile at $U = 2.00$ V, which is equal to the valence band-edge potential of a GaN/ZnO solid solution at Zn/Ga=0.42[85]. The first reaction is uphill in free energy, and the following steps are all downhill. Under the operating condition of a ZnO/GaN solid solution photocatalyst, the first reaction is again likely to be the rate-limiting step. One thing to notice in Fig. 4.3 is that, for $U = 2.00$ V (red) line, the free energy of the $*OOH^-$ system is lower than that of the starting $*OH^-$ system (starting point). For $U > 2.00$ V (between the black and red lines), its free energy is even lower. This suggests that the valence band-edge potential of the GaN/ZnO alloy might be sufficient to drive the two-electron process $*OH^- + H_2O \rightarrow *OOH^- + 2e^- + 2H^+$ (standard

potential 1.92 V), and the entire catalytic cycle would consist of exothermic steps. We speculate that this two-electron process might be important for the water oxidation on the surface of the GaN/ZnO solid solution.

4.3.4 Standard Reduction Potentials

The standard reduction potentials for our four reaction steps are calculated by: $E^{\mathrm{o}} = -\Delta G_{\mathrm{R}}/nF$, where ΔG_{R} is the Gibbs free energy change relative to NHE in the reduction reaction, and equals $-\Delta G_i$ $(i = 1, 2, 3, 4)$ in the previous section. Here n is the number of electrons involved in the step and is 1 in one-electron steps. The calculated values for all four one-electron reactions, and possible two-electron reactions, are shown in the left of Table 4.2. It is interesting to mention that for all steps in our mechanism on the GaN surface, there are analogous reactions in aqueous solution, and their standard reduction potentials are similar. In some sense, in our mechanism the surface Ga acts like a hydrogen ion (proton) in a water molecule. When a water molecule dissociates on the surface of GaN, a surface Ga replaces hydrogen in the water and forms a stable bond with oxygen. This Ga-O bond only breaks at the last step of oxidation when an O_2 molecule is formed. We speculate that this picture could be valid on other semiconductor photo-catalyst surfaces, so our reaction mechanism and analysis might apply more generally than just to the system considered here. The reaction energetics, however, would vary from one system to another depending mainly on the details of the surface cation-oxygen interaction.

It should be mentioned that the electron withdrawing effect of the passi-

vating fluorine atoms on the Ga electon density is unknown, and might well change the calculated reduction potentials. We also face two intrinsically difficult problems. The first problem is that, when calculating the free energies of the intermediates, the vibrational frequencies of the model (including the explicit water molecules which represent part of the bulk water) were calculated at their zero temperature geometries as harmonic oscillators. This approach works well for a harmonic solid but may not accurately describe the free energy of a solid/liquid interface. The second problem is that, to get the free energy of each intermediate, strictly speaking, we should find all the energy-minimized structures (local minima) of the corresponding model and do a Boltzmann average of them. We have simplified this procedure to only using the lowest energy structure. However, even finding that is a difficult task. Best efforts have been made to obtain the lowest energy structures of the intermediates.

4.4 Summary

Our calculations confirm a feasible mechanism for water oxidation on a GaN $(10\bar{1}0)$ surface, using a cluster model to simulate the GaN/aqueous interface and for calculating the energetics. According to our calculations, a mechanism for water oxidation starts with a hydroxide ion attached to a surface Ga site: $^*OH^-$. This is sequentially oxidized to $^*O^{\bullet -}$, $^*OOH^-$, $^*O_2^{\bullet -}$ and O_2 gas in four sequential proton-coupled electron-transfer steps. This can account for water oxidation of GaN in the presence of a sacrificial electron acceptor. The step requiring the highest potential is predicted to be the first step, in which

$^*OH^-$ is oxidized into $^*O^{\bullet-}$. A potential of 2.81 V is required to drive this step, which is close to the experimental valence band-edge potential of GaN. The lower valence-band potential of GaN/ZnO solid solution may require a two-electron step in which $^*OH^-$ goes directly to $^*OOH^-$.

Chapter 5

Stability of 1D ZnO nanostructure

5.1 Introduction

ZnO is an important material because of its electron mobility, wide band gap, and large exciton binding energy. ZnO nanostructures such as nanowires, nanotubes, and nanobelts are promising building blocks for optical, electronic, and chemical sensing devices[86–88]. Several synthetic routes have yielded multiwalled ZnO nanotubes[89–96]. These tubes are 20- 450 nm in diameter and have wall thicknesses of 4-100 nm. No single-walled ZnO nanotubes (SWZONTs) have been reported experimentally, although some groups have predicted their properties theoretically[97, 98]. Ref [98] also suggested some applications of SWZONTs. Recently, sequences of $(ZnO)^n$ clusters were studied by B. L. Wang et al.[99]. They found that tubular structures are metastable for $(ZnO)_n$ $(n = 9 - 18)$ and suggested that ZnO nanotubes resemble C or

BN nanotubes. Here we calculate the energy of small ZnO nanowires and SWZONTs with same number of atoms, and find that SWZONTs are energetically more stable at small size. This provides a new guideline for making SWZONTs.

5.1.1 Calculation

Our nanowires are fragments of wurtzite ZnO, cut along the (001) axis with period c. They have 12, 20, 26, 32, and 48 atoms per unit cell, corresponding to C_{6V}, C_{2V}, C_{3V}, C_{2V}, and C_{6V} symmetries (see Figure 5.1). The SWZONTs are all the zigzag type, which has the same periodicity as the nanowires. We consider the (3,0), (5,0), (6,0), (7,0), (8,0), and (12,0) nanotubes, which correspond to 12, 20, 24, 28, 32, and 48 atoms per unit cell. The surface atoms are not saturated by foreign atoms. Figure 5.1 shows the cross sections of calculated nanowires and nanotubes. The calculation uses the plane-wave pseudopotential method, density functional theory (DFT), and the Quantum Espresso/PWSCF code[50]. We use Vanderbilt ultrasoft pseudopotentials[51] with the Perdew-Burke-Ernzerhof (PBE)[22] version of the generalized gradient approximation (GGA) exchange-correlation functional. The Zn 4s and 3d states and O 2p and 2s states are treated as valence electrons. The cutoff of kinetic energy is 30 Ry, while the cutoff of charge density is 300 Ry. The Broyden-Fletcher-Goldfarb-Shanno (BFGS)[69] method is used for geometry optimization. A $5 \times 5 \times 5$ k-point mesh is used to test the ZnO bulk properties, and a $1 \times 1 \times 10$ mesh is used for the nanowire and nanotube. We apply Gaussian broadening with smearing parameter 0.002 Ry. The force on each

Table 5.1: Comparison between our bulk results and other GGA calculation and experiments

	Present Work	Other GGA	Experiment
a(Å)	3.292	3.383[100]	3.250[101]
c(Å)	5.309	5.289[100]	5.207[102]
u^a	0.3793	0.378[100], 0.3790[103]	0.3817[104]
E_{coh}(eV/f.u.)	7.27	7.692[103]	7.56[104]
B_0(GPa)	127	149[100], 133.7[103]	142.6[104]
Badn Gap(eV)	0.71	0.75[100]	3.4[105]

[a] The spacing between closest Zn and O layers is $(1/2 - u)c$.

atom is converged to 0.003 eV/Åfor all optimizations. We arranged the ZnO nanowires and tubes in a 2D hexagonal supercell and separated them by at least 8 Å. Both internal coordinates of atoms and the lattice constant c are relaxed.

5.2 Results

5.2.1 Bulk Property

The calculated bulk properties are in Table 5.1 and agree with other GGA calculations, although our results show slightly more underbinding. This may come from ultrasoft pseudopotentials because the plane-wave cutoff and k-point sampling convergence are well tested. Our lattice parameters are 2% larger than the experimental values, which is usual for GGA calculations.

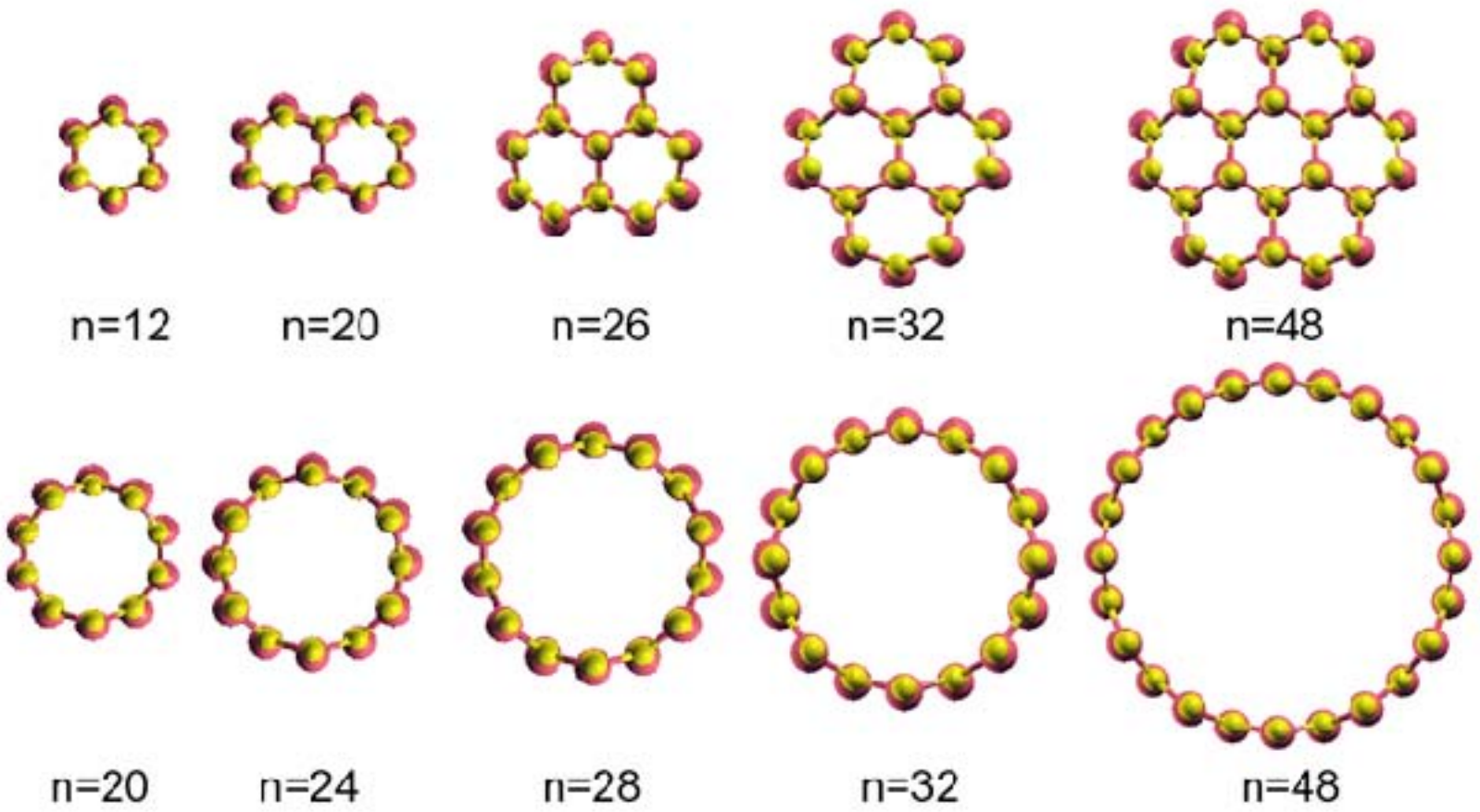

Figure 5.1: Calculated ZnO nanowires and SWZONTs. Small yellow balls represent Zn atoms, and large orange balls represent O atoms. n is the number of atoms in one periodic unit.

Both wires and tubes are semiconducting, but the theoretical gap is far too small, as is also true for bulk ZnO (see Table 5.1). Previous work[97] calculated the (4,4) armchair SWZONT and suggested that armchair SWZONTs act like conductors. We tested this and found a positive band gap similar to zigzag SWZONTs.

5.2.2 Energetics of Nanowires and Nanotubes

In our calculation, the nanowires are pieces of bulk ZnO. The exposed surfaces correspond to $(10\bar{1}0)$ and $(11\bar{2}0)$ nonpolar surfaces of wurtzite ZnO. For a review of ZnO surfaces, see ref 18. One issue that may arise is whether there could be surface reconstructions apart from ordinary relaxations. To the best of our knowledge, for those surfaces, no reconstructions are reported, except (1×1), whose features are the tilting and contraction of surface Zn-O bonds, which are also observed in our calculation. We also did a direct test for the possibility of a (1×2) surface reconstruction in $n = 26$ nanowire. We took a fully relaxed nanowire, doubled the unit cell along the c-axis, and gave every atom a random displacement between 0 and 0.2 Å. For three different starting displacements, the final geometry is the same as the undisplaced one. No dimerization is observed.

The first nanowire (12 atoms per unit cell) is also the first nanotube. For the second nanowire (two honeycomb units, 20 atoms per cell), we found that the nanowire structure is higher in energy than the SWZONT. To test whether the relative stability depends on the choice of exchangecorrelation functional, we changed GGA to LDA (Perdew- Zunger)[20] for the 20 atoms per cell C_{2V}

Table 5.2: Values of n_d for some typical n

n	12	20	26	32	48
n_d	12	16	18	20	24

nanowire and (5,0) nanotube. The results show that the SWZONT is indeed more stable, although the difference of energies changed from ∼90 to ∼60 meV. Figure 5.2 shows the total energy (measured from the global minimum, E_0) vs lattice parameter c for both GGA and LDA results.

Larger nanowires and SWZONTs are also calculated. The final energies of relaxed nanowires and nanotubes are plotted in Figure 5.3. It shows that, for 1D ZnO structures (<38 atoms per unit cell), the SWZONT is energetically more favorable than the crystal-like nanowire form. This can be understood if we view ZnO bonds as covalent. The wurtzite ZnO crystal has σ bonds made from sp^3 hybrid orbitals. Small nanowires have dangling bonds on the surface that increase the energy. In a nanotube, as in a graphene-like planar sheet, π bonds resulting from sp^2 hybridization will form, lowering the energy. As the wire grows larger, the fraction of surface dangling bonds decreases and the fraction of saturated sp^3 σ bonds increases, so the wire will eventually have lower energy than the SWNT.

The total energy $E_{\mathrm{NT}}(n)$ of a SWZONT with n atoms in the unit cell can be written as the sum of total energy of graphene-like planar ZnO sheet E_{sheet} and a strain energy $E_{\mathrm{strain}}(n)$ related to tube curvature,

$$E_{\mathrm{NT}}(n) = E_{\mathrm{sheet}} + E_{\mathrm{strain}}(n)$$

For a single-layer planar ZnO sheet, we find $E_{\mathrm{sheet}} = 400\mathrm{meV/pair}$ relative

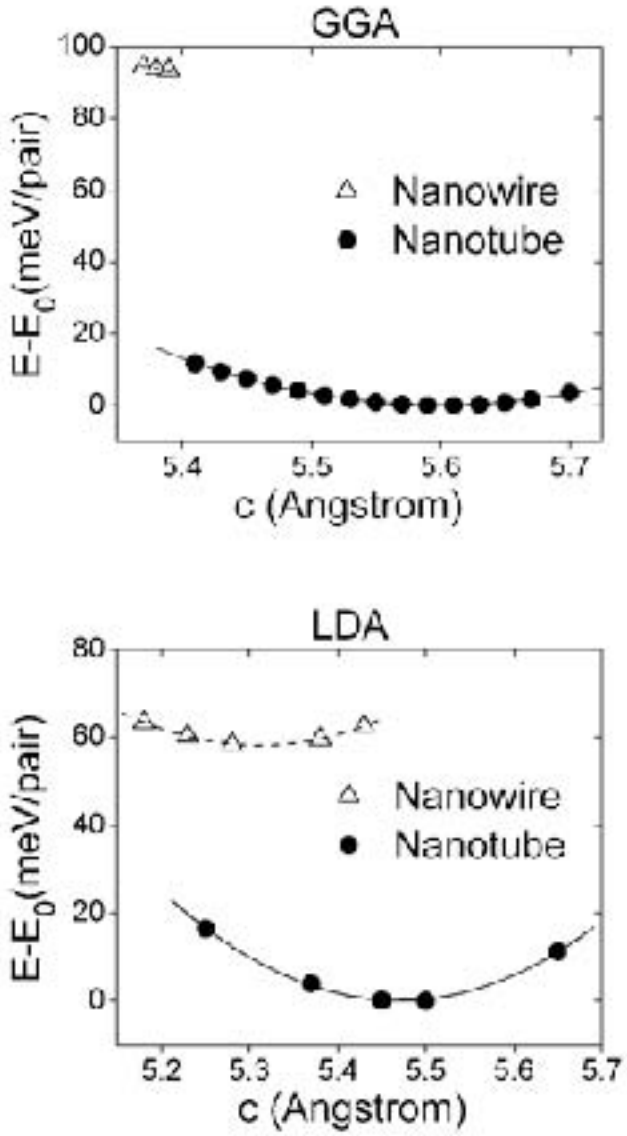

Figure 5.2: Energy vs c for 20 atom unit cell ZnO nanowire and SWZONT. (GGA and LDA). In GGA calculation, the nanowire relaxes into a nanotube when lattice parameter c is increased; in LDA calculation, the nanowire is metastable.

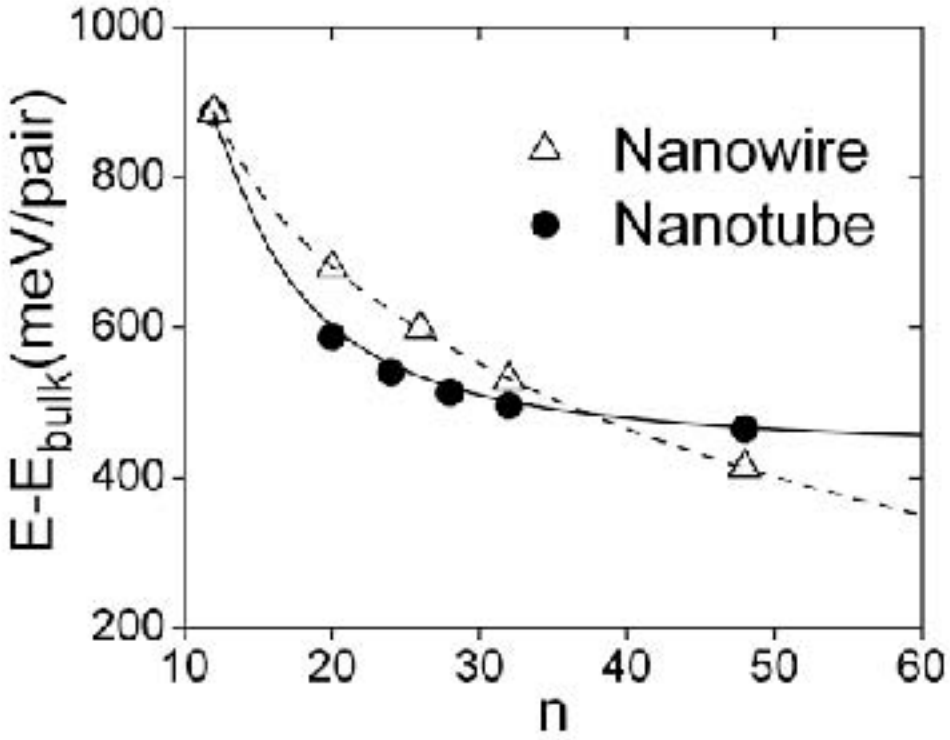

Figure 5.3: Relative energy for SWZONTs and nanowires from DFT results. The dashed line is just a guide to the eye that represents nanowires and converges to the ZnO bulk value. The solid line represents SWZONTs, is fitted to $1/n^2$, and converges to the graphene-like ZnO planar sheet.

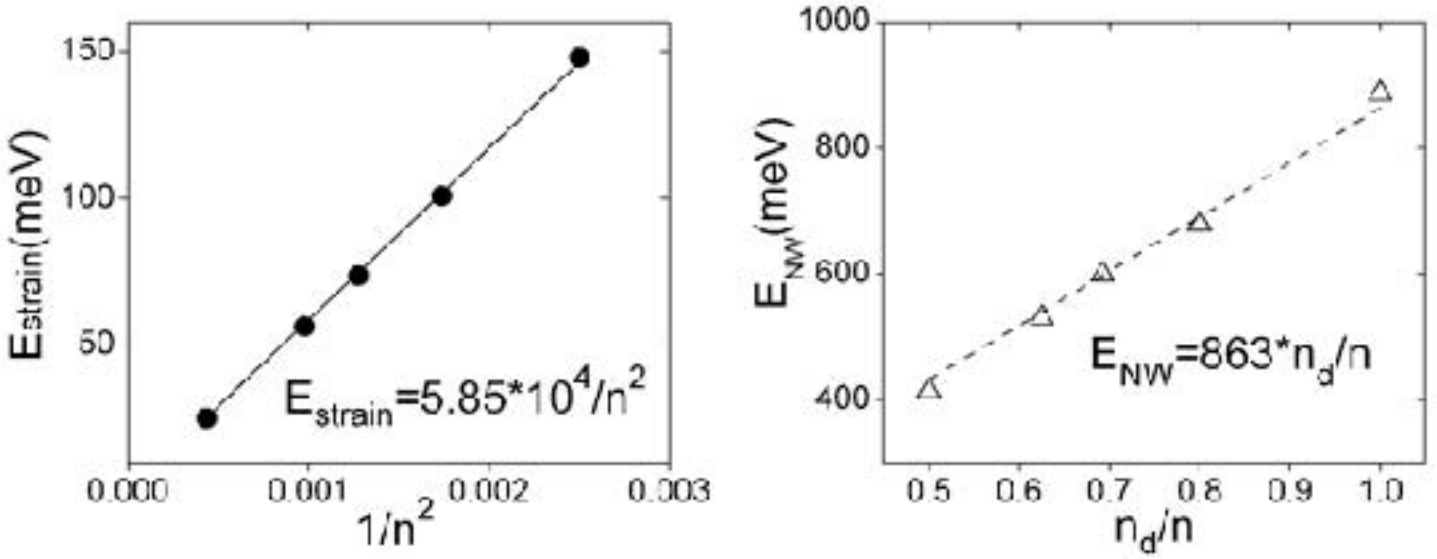

Figure 5.4: Fitting of the strain energy of SWZONT as a function of $1/n^2$ (left) and the ZnO nanowire energy as a function of n_d/n (right).

to bulk ZnO. The strain energy for a nanotube is related to radius R by $E_{\text{strain}}(n) \approx c/R^2$[106]. The diameter of a SWZONT is approximately proportional to n, so

$$E_{\text{strain}}(n) \approx c/n^2$$

By fitting DFT data points (see Figure 5.4, left panel), we obtain the strain energy:

$$E_{\text{strain}}(n) = 5.85 \times 10^4/n^2 \text{ meV/pair}$$

Therefore, the total energy of a SWZONT is

$$E_{\text{NT}}(n) = 440 + 5.85 \times 10^4/n^2 \text{ meV/pair}$$

The total energy of a ZnO nanowire can be approximated as

$$E_{\text{NW}}(n) = \frac{n_d}{n}E_d + \frac{n_b}{n}E_b$$

where E_d is the energy of a pair of Zn and O atoms with each having a dangling bond, E_b is the total energy of bulk ZnO, n_d/n and n_b/n are the fraction of atoms with and without dangling bonds. The value of n_d for some typical n are listed in Table 5.2. Taking $E_b = 0$ and fitting the DFT data (Figure 5.4, right panel), we get E_d =863 meV/pair and the total energy of a ZnO nanowire is

$$E_{\text{NW}}(n) = \frac{n_d}{n}E_d = 863\frac{n_d}{n} \text{ meV/pair}$$

On the basis of the models above, the critical number of atoms when phase

transition (nanotube to nanowire) occurs is $n \sim 40$, which agrees well with previous value $n \sim 38$, estimated directly from the DFT calculation.

Similar to the BN nanotube[107], there is some buckling on the surface of the ZnO nanotube, i.e., the cylinder formed by O atoms has a larger diameter than the cylinder formed by Zn atoms (see Figure 5.1). It is shown in Figure 5.5 that, as the size of the SWZONT increases, the buckling distance ΔR (the radius difference of O and Zn cylinders) decreases as $1/n$ (or $1/R$) and eventually goes to zero when the tube becomes a flat sheet. This behavior is also observed in BN nanotubes, where it was explained by the different hybridizations of B and N atoms[107, 108]. Here we offer a slightly different interpretation. Covalent bond-bending interactions try to keep the Zn and O cylinder radii R equal, with a restoring force $-k\Delta R$ per pair. The reason O atoms prefer a larger cylinder than Zn atoms is Fermi pressure. The HOMO levels are based on oxygen p orbitals. In common with free electrons, their energies increase toward the Fermi level because of increased kinetic energy to a value $E_F \propto \hbar^2[1/m_a\lambda_a^2 + 1/m_c\lambda_c^2]$ per pair, where the Fermi energy depends on m_a and m_c, band effective masses perpendicular and parallel to c, and λ_a and λ_c, the Fermi wavelengths in the two directions, which are fixed by the geometry of the atoms. Specifically, $\lambda_a \propto R/n$ and $\lambda_c \propto c$. Thus there is an outward force $-dE_F/dR \propto n^2/R^3 \propto 1/R$, where the last substitution follows because $n \propto R$. The force balance gives $\Delta R \propto 1/R \propto 1/n$, that is, the oxygen-zinc radial spacing falls off as $1/n$, as is seen roughly in Figure 5.5.

To make SWZONTs, they need to be very small. One way to do this is inhibiting radial growth by confinement of the SWZONT in a narrow cylindrical channel, as was done for ultrathin carbon nanotubes[109]. Extra-large pore

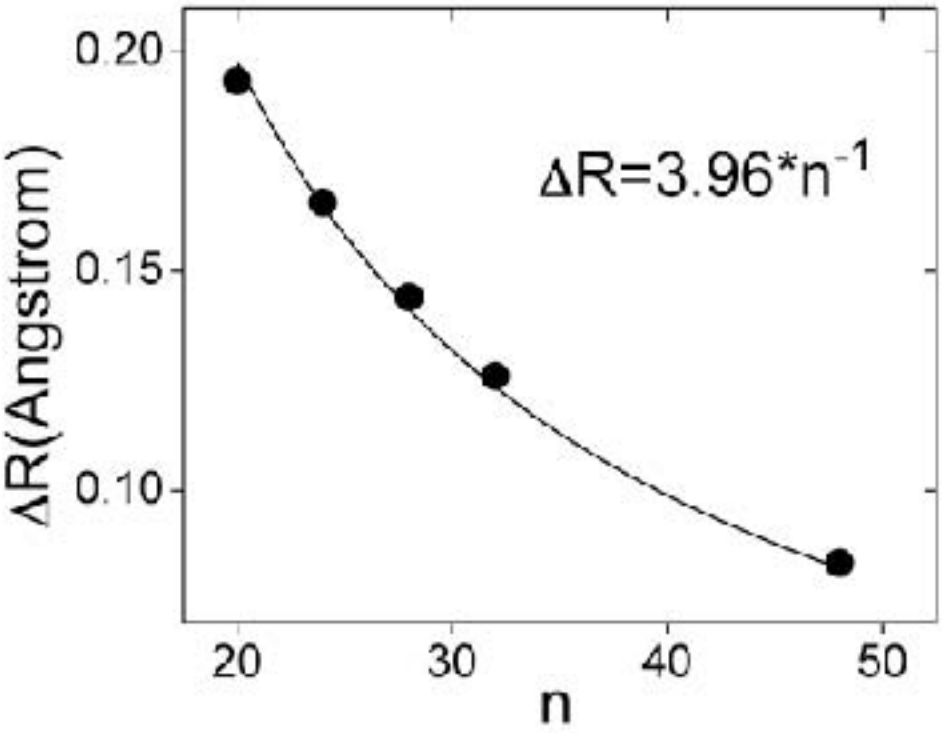

Figure 5.5: Buckling distance ΔR (the radius difference of O and Zn cylinders) vs the number of atoms per unit cell of a SWZONT. The solid line is a fit to 1/n.

zeolites such as VPI-5[110] might be used to control the size of SWZONTs. If ultrasmall catalyst particles can be made, a catalyst growth mechanism similar to ref cata-growth may also work for ZnO. The other growth strategy is to prevent the radial collapse of SWZONTs by growing them on the outer surface of other 1D nano structures such as metal nanowires (similar to ref [92] or carbon nanotubes (as suggested by ref [98]).

5.2.3 Effect of Vibrational Entropy

In the present calculation, no foreign molecules passivate the surface, and all calculations are at zero temperature. In experiment, passivation may occur, and the temperature will be hundreds of Kelvin. Passivation favors the nanowire structure because the energy of the dangling bond gets lowered. High temperature favors the nanotube structure because it has larger vibrational entropy due to radial softness, which leads to low-frequency radial modes, especially a doubly degenerate very soft radial mode where the tubes cross section deforms into an ellipse. The total free energy lowering $T\Delta S$ for the $n = 32$ tube compared with the $n = 32$ wire is roughly $10k_BT$ with an uncertainty $\sim 20\%$. This estimate uses the high-temperature formula $S_i \approx k_B\ln(k_BT/\omega_i)$ for the entropy of the ith harmonic oscillator, where $k_B\ln T$ is the classical answer, independent of frequency, and $-k_B\ln\omega_i$ is the quantum correction. Thus the free energy difference $\Delta F = F^{\mathrm{NT}} - F^{\mathrm{NW}}$ contains a term $-T(\Delta S^{\mathrm{NT}} - \Delta S^{\mathrm{NW}}) \approx k_BT\sum_i \ln(\omega_i^{\mathrm{NT}}/\omega_i^{\mathrm{NW}})$ which favors lower frequencies. The vibrational frequencies at $q = 0$ for $n = 32$ tube and wire (Figure 5.6), as calculated using Quantum Espresso, are used as ω_i. It is somewhat surprising

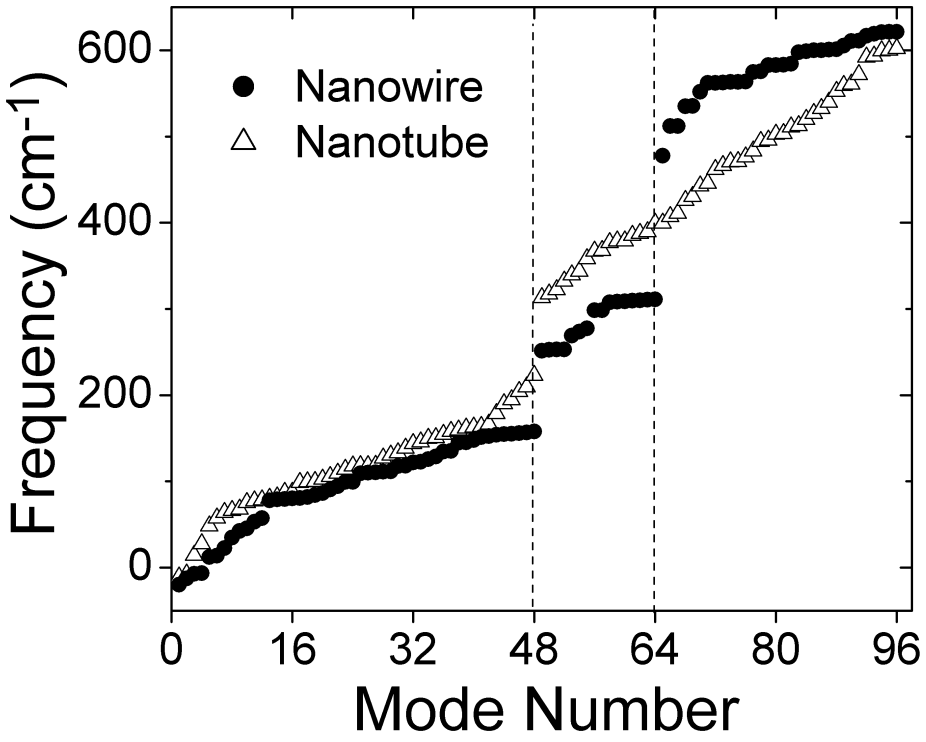

Figure 5.6: Phonon frequencies of all 96 modes at $q = 0$ for $n = 32$ nanowire and nanotube. The small negative frequencies of several lowest modes come from incomplete relaxation, tube-tube, or wire-wire interactions between periodic images and other uncertainties in the calculation. The gap around 250 cm^{-1} in the wire reflects the gap in mid-spectrum for vibrations in bulk ZnO[111]. The extra gap around 400 cm^{-1} in the tube occurs at exactly the 2/3 point of the spectrum, where we believe the optical branches of the two-dimensional graphene-like ZnO sheet are split into 1/3 lower lying perpendicular optic modes and 2/3 higher lying parallel optic modes.

how small the entropy enhancement is for the tube. To a large degree, in the optical branches (modes 49-96 in Figure 5.6), the softness of lowlying radial modes (49 to 64) of the tube is compensated by stiffness of the high-lying bond-stretching axial and tangential modes (65-96). In the acoustic branches, the softness is not compensated, and the free energy gets lowered.

5.3 Afterword

So far Chapter 5 is a verbatim copy of Nano Letters vol. 7, p. 2267-2271. This section adds a few words. The single-walled ZnO nanotubes (SWZONTs) haven't been realized experimentally at the time this thesis is written. However, in an experimental paper published right after our work, a two-monolayer-thick ZnO film grown on the Ag (111) surface was found to have the hexagonal planar structure[112]. This planar structure is closely related to our proposed ZnO single-walled nanotube (corresponding to $R = \infty$). This discovery is encouraging news for making SWZONTs, especially through the routes of growing them on the outer surface of metal nanowires or carbon nanotubes.

Bibliography

[1] K. Maeda, T. Takata, M. Hara., N. Saito, Y. Inoue, H. Kobayashi, and K. Domen. *J. Am. Chem. Soc.*, 127:8286, 2005.

[2] K. Maeda, K. Teramura, T. Takata, M. Hara., N. Saito, K. Toda, Y. Inoue, H. Kobayashi, and K. Domen. *J. Phys. Chem. B*, 109:20504, 2005.

[3] K. Maeda, K. Teramura, D. Lu, T. Takata, N. Saito, Y. Inoue, and K. Domen. *Nature*, 440:295, 2006.

[4] L. L. Jensen, J. T. Muckerman, and M. D. Newton. *J. Phys. Chem. C*, 112:3439, 2008.

[5] S. H. Wei and A. Zunger. *Phys. Rev. B*, 37:8958, 1988.

[6] K. Maeda, K. Teramura, and K. Domen. *J. Catal.*, 254:198, 2008.

[7] A. Fujishima and K. Honda. *Nature*, 238:37, 1972.

[8] K. Maeda, K. Teramura, N. Saito, Y. Inoue, and K. Domen. *Bull. Chem. Soc. Jpn.*, 5:1004–1010, 2007.

[9] W. Qian, M. Skowronski, K. Doverspike, L. B. Rowland, and D. K. Gaskill. *J. Cryst. Growth*, 151:396, 1995.

[10] W. Qian, G. Rohrer, M. Skowronski, K. Doverspike, L. B. Rowland, and D. K. Gaskill. *Appl. Phys. Lett.*, 67:2284, 1995.

[11] P. Vennegues, B. Beaumont, M. Vaille, and P. Gibart. *J. Cryst. Growth*, 173:249, 1997.

[12] P. Vennegues, B. Beaumont, M. Vaille, and P. Gibart. *Appl. Phys. Lett.*, 70:2434, 1997.

[13] D. Cherns, W. T. Young, J. W. Steeds, F. A. Ponce, and S. Nakamura. *J. Cryst. Growth*, 178:201, 1997.

[14] B. Meyer, D. Marx, O. Dulub, U. Diebold, M. Kunat, D. Langenberg, and C. Woll. *Angew. Chem. Int. Ed.*, 43:6641, 2004.

[15] X. Shen, P. B. Allen, M. S. Hybertsen, and J. T. Muckerman. *J. Phys. Chem. C*, 113:3365–3368, 2009.

[16] P. Hohenberg and W. Kohn. *Phys. Rev.*, 136:B864, 1964.

[17] W. Kohn and L. J. Sham. *Phys. Rev.*, 140:A1133, 1965.

[18] N. W. Ashcroft and N. D. Mermin. *Solid State Physics*. Holt, Rinehart and Winston, 1976.

[19] D. M. Ceperley and B. J. Alder. *Phys. Rev. Lett.*, 45:566, 1980.

[20] J. P. Perdew and A. Zunger. *Phys. Rev. B*, 23:5048, 1981.

[21] S. H. Vosko, L. Wilk, and M. Nusair. *Can. J. Phys.*, 58:1200, 1980.

[22] J. P. Perdew, K. Burke, and M. Ernzerhof. *Phys. Rev. Lett.*, 77:3865, 1996.

[23] A. D. Becke. *Phys. Rev. A*, 38:3098–3100, 1988.

[24] C. Lee, W. Yang, and R. G. Parr. *Phys. Rev. B*, 37:785–789, 1988.

[25] B. Miehlich, A. Savin, H.Stoll, and H. Preuss. *Chem. Phys. Lett.*, 157: 200–206, 1989.

[26] A. D. Becke. *J. Chem. Phys.*, 98:1372, 1993.

[27] P. J. Stephens, F. J. Devlin, C. F. Chabalowski, and M. J. Frisch. *J. Phys. Chem.*, 98:11623, 1994.

[28] A. D. Becke. *J. Chem. Phys.*, 98:5648, 1993.

[29] *J. Chem. Phys.*, 53:2823, 1970.

[30] T. H. J. Dunning and P. J. Hay. *Modern Theoretical Chemistry*. Plenum, New York, 1976.

[31] S. Miertus, E. Scrocco, and J. Tomasi. *Chem. Phys.*, 55:117, 1981.

[32] A. Klamt and G. J. Schuurmann. *J. Chem. Soc., Perkin Trans.*, 799: 805, 1993.

[33] R. A. Pierotti. *Chem. Rev.*, 76:717, 1976.

[34] F. M. Floris and J. Tomasi. *J. Comput. Chem.*, 10(616), 1989.

[35] F. M. Floris, J. Tomasi, and J. L. Pascul-Ahuir. *J. Comput. Chem.*, 12: 784, 1991.

[36] J. Caillet and P. Claverie. *Acta Crystallogr. B*, 34:3266, 1978.

[37] J. Tomasi, B. Mennucci, and R. Cammi. *Chem. Rev.*, 105:2999, 2005.

[38] J. L. Pascul-Ahuir and E. Silla. *J. Comput. Chem.*, 11:1047, 1990.

[39] E. Silla, F. Villar, O. Nilsson, J. L. Pascul-Ahuir, and O. Tapia. *J. Mol. Graph.*, 8:168, 1990.

[40] E. Silla, I. Tunon, and J. L. Pascul-Ahuir. *J. Comput. Chem.*, 12:1077, 1991.

[41] V. Barone, M. Cossi, and J. Tomasi. *J. Chem. Phys.*, 107:3210, 1997.

[42] Y. Takano and K. N. Houk. *J. Chem. Theory Comput.*, 1:70–77, 2005.

[43] D. M. MacQuarrie. *Statistical Mechanics*. Harper and Row, New York, 190.

[44] O. Dulub, B. Meyer, and U. Diebold. *Phys. Rev. Lett.*, 95:136101, 2005.

[45] B. Meyer, H. Rabaa, and D. Marx. *Phys. Chem. Chem. Phys.*, 8:1513, 2006.

[46] Y. Yan and M. M. Al-Jassim. *Phys. Rev. B*, 72:235406, 2005.

[47] V. M. Bermudez and J. P. Long. *Surface Science*, 450:98, 2000.

[48] B. Meyer and D. Marx. *Phys. Rev. B*, 67:035403, 2003.

[49] J. E. Northrup and J. Neugebauer. *Phys. Rev. B*, 53:R10477, 1996.

[50] S. Baroni, A. D. Corso, S de Gironcoli, and P. Giannozzi. URL http://www.quantum-espresso.org.

[51] D. Vanderbilt. *Phys. Rev. B*, 41:7892, 1990.

[52] H. Schulz and K. H. Thiemann. *Solid State Commun.*, 23:815, 1977.

[53] M. Leszczynski et al. *Appl. Phys. Lett.*, 69:73, 1996.

[54] W. A. Harrison. *Electronic Structure and the Properties of Solids*. Dover Publications, New York, 1989.

[55] P. Perlin, C. Jauberthie-Carillon, J. P. Itie, A. San Miguel, I. Grzecory, and A. Wlian. *High Press. Research*, 7:96, 1991.

[56] P. Perlin, C. Jauberthie-Carillon, J. P. Itie, A. San Miguel, I. Grzegory, and A. Polian. *Phys. Rev. B*, 45:83, 1992.

[57] H. Xia, Q. Xia, and A. L. Ruoff. *Phys. Rev. B*, 47:12925, 1993.

[58] M. Ueno, M. Yoshida, A. Onodera, O. Shimomura, and K. Takemura. *Phys. Rev. B*, 49:14, 1994.

[59] R. C. Powell, N.-E. Lee, Y.-W. Kim, and J. E. Greene. *J. Appl. Phys.*, 73:189, 1993.

[60] W. S. Benedict, N. Gailar, and E. K. Plyler. *J. Chem. Phys.*, 24:1139, 1956.

[61] S. A. Clough, Y. Beers, G. P. Klein, and L. S. Rothman. *J. Chem. Phys.*, 59:2254, 1973.

[62] C. Stampfl and C. G. Van de Walle. *Phys. Rev. B*, 59:5521, 1999.

[63] A. Zoroddu, F. Bernardini, P. Ruggerone, and V. Fiorentini. *Phys. Rev. B*, 64:045208, 2001.

[64] M. Sprik, J. Hutter, and M. J. Parrinello. *J. Chem. Phys.*, 105:1142, 1996.

[65] E. Schwegler, J. C. Grossman, F. Gygi, and G. Galli. *J. Chem. Phys.*, 121:5400, 2004.

[66] M. V. Fernandez-Serra and Emilio Artacho. *J. Chem. Phys.*, 121:11136, 2004.

[67] G. Henkelman and H. Jonsson. *J. Chem. Phys.*, 113:9978, 2000.

[68] G. Henkelman, B. P. Uberuaga, and H. Jonsson. *J. Chem. Phys.*, 113: 9901, 2000.

[69] W. H. Press, S. A. Teukolsky, W. T. Vetterling, and B. P. Flannery. *Numerical Recipes*. Cambridge University Press, Cambridge, 3rd edition, 2007.

[70] C.-L. Fu and K.-M. Ho. *Phys. Rev. B*, 28:5480, 1983.

[71] F. D. Murnaghan. *Natl. Acad. Sci. USA*, 30:244, 1944.

[72] H. C. Hamaker. *Physica*, 4:1058, 1937.

[73] J. Lyklema. *Fundamentals of Interface and Colloid Science*, volume 1. Academic Press, London, 1991.

[74] A Dal Corso and E. Tosatti. *Phys. Rev. B*, 47:9742, 1993.

[75] V. A. Parsegian and G. H. Weiss. *J. of Colloid Interface Sci.*, 81:285, 1981.

[76] A. Valdes, Z.-W. Qu, G.-J. Kroes, J. Rossmeisl, and J. K. Norskov. *J. Phys. Chem. C*, 112:9872, 2008.

[77] M. J. Frisch et al. *Gaussian03*. Gaussian Inc., Wallingford, CT, revision e.01 edition, 2004.

[78] P. J. Hay and W. R. Wadt. *J. Chem. Phys.*, 82:270–283, 1985.

[79] P. J. Hay and W. R. Wadt. *J. Chem. Phys.*, 82:299–310, 1985.

[80] W. R. Wadt and P. J. Hay. *J. Chem. Phys.*, 82:284–298, 1985.

[81] M. D. Tissandier, K. A. Cowen, W. Y. Feng, E. Gundlach, M. H. Cohen, A. D. Earhart, J. V. Coe, and T. R. Tuttle. *J. Phys. Chem. A*, 102:7787, 1998.

[82] A. J. Bard, R. Parsons, and J. Jordan, editors. *Standard Potentials In Aqueous Solution*. Marcel Dekker, New York, 1985.

[83] I. M. Huygens, K. Strubbe, and W. P. Gomes. *J. Electrochem. Soc.*, 147: 1797–1802, 2000.

[84] J. D. Beach, R. T. Collins, and J. A. Turner. *J. Electrochem. Soc.*, 150: A899–A904, 2003.

[85] H. Hashiguchi, K. Maeda, R. Abe, A. Ishikawa, J. Kubota, and K. Domen. *Bull. Chem. Soc. Jpn.*, 82:401–407, 2009.

[86] Z. Fan and J. G. Lu. *Nanosci. Nanotechnol.*, 5:1561, 2005.

[87] Y. Y. Wu and P. D. Yang. *J. Am. Chem. Soc.*, 123:3165, 2001.

[88] Z. L. Wang. *J. Phys.: Condes. Matter*, 16:R829, 2004.

[89] J. Zhang, L. Sun, C. Liao, and C. Yan. *Chem. Commun*, 3:262, 2002.

[90] J. J. Wu, S. C. Liu, C. T. Wu, K. H. Chen, and L. C. Chen. *Appl. Phys. Lett.*, 81:1312, 2002.

[91] J. Q. Hu, Q. Li, X. M. Meng, C. S. Lee, and S. T. Lee. *Chem. Mater.*, 15:305, 2003.

[92] X. H. Zhang, S. Y. Xie, Z. Y. Jiang, X. Zhang, Z. Q. Tian, Z. X. Xie, R. B. Huang, and L. S. Zheng. *J. Phys. Chem. B*, 107:10114, 2004.

[93] Y. J. Xing, Z. H. Xi, Z. Q. Xue, X. D. Zhang, J. H. Song, R. M. Wang, J. Xu, Y. Song, S. L. Zhang, and D. P. Yu. *Appl. Phys. Lett.*, 83:1689, 2003.

[94] X. H. Kong, X. M. Sun, X. L. Li, and Y. D. Li. *Mater. Chem. Physics*, 82:997, 2003.

[95] X. Y. Kong, Y. Ding, and Z. L. Wang. *J. Phys. Chem. B*, 108:570, 2004.

[96] Y. Sun, G. M. Fuge, N. A. Fox, D. J. Riley, and M. N. R. Ashfold. *Adv. Mater.*, 17(2477), 2005.

[97] S. Erkoc and H. Kokten. *Physica E*, 28:162, 2005.

[98] Z. C. Tu and X. Hu. *Phys. Rev. B*, 74:035434, 2006.

[99] B. L. Wang, S. Nagase, J. J. Zhao, and G. H. Wang. *J. Phys. Chem. C*, 111:4956, 2007.

[100] P. Erhart, K. Albe, and A. Klein. *Phys. Rev. B*, 73:205203, 2006.

[101] E. H. Kisi and M. M. Elcombe. *Acta Crystallog*, C45:1867, 1989.

[102] *CRC Handbook of Chemistry and Physics*. CRC, Boca Raton, FL, 58th edition, 1977.

[103] J. E. Jaffe, J. A. Snyder, Z. Lin, and A. C. Hess. *Phys. Rev. B*, 62:1660, 2000.

[104] S. Desgreniers. *Phys. Rev. B*, 58:14102, 1998.

[105] O. Madelung, editor. *Landolt-Bornstein, Numerical Data and Fucntional Relationships in Science and Technology*, volume 17, part b of *New Series, Group III*. Springer-Verlag, Berlin, 1982.

[106] D. H. Robertson, D. W. Brenner, and J. W. Mintmire. *Phys. Rev. B*, 45:12592, 1992.

[107] X. Blase, A. Rubio, S. G. Louie, and M. L. Cohen. *Europhys. Lett.*, 28: 335, 1994.

[108] L. Wirtz, A. Rubio, R. A. de la Concha, and A. Loiseau. *Phys. Rev. B*, 68:045425, 2003.

[109] N. Wang, Z. K. Tang, G. D. Li, and J. S. Chen. *Nature*, 408:50, 2000.

[110] M. E. Davis, C. Saldarriaga, C. Montes, J. Carces, and C. Crowder. *Nature*, 331:698, 1988.

[111] J. Serrano, A. H. Romero, F. J. Manjon, R. Lauck, M. Cardona, and A. Rubio. *Phys. Rev. B*, 69:094306, 2004.

[112] C. Tusche, H. L. Meyerheim, and J. Kirschner. *Phys. Rev. Lett.*, 99: 026102, 2007.